

An Imperative study of the angular observables in $\Lambda_b^0 \rightarrow \Lambda_c^+(\rightarrow \Lambda\pi^+)\tau\bar{\nu}_\tau$ decay and probing the footprint of new physics

Soumitra Nandi^a Shantanu Sahoo^a Ria Sain^a

^aIndian Institute of Technology, North Guwahati, Guwahati 781039, Assam, India

E-mail: soumitra.nandi@iitg.ac.in, shantanu.sahoo@iitg.ac.in,
riasain@rnd.iitg.ac.in

ABSTRACT: We study the 4-body angular distribution for $\Lambda_b \rightarrow \Lambda_c^+(\rightarrow \Lambda\pi^+)\ell^-\bar{\nu}$ decays and find out the analytical expressions for various asymmetric and angular observables in the Standard Model and the new physics scenarios and compared them with the literature. Using the available inputs from the lattice, we have predicted the values with uncertainties of all these observables in the Standard Model. Considering the new physics effects in $b \rightarrow c\tau^-\bar{\nu}_\tau$ transitions, we have constrained the new Wilson coefficients of the one operator and two operator scenarios from the available data on these decays. The two-operator scenario with scalar-pseudoscalar and tensor quark current provides the most plausible solution to the current data. Also, we have tested the new physics sensitivities (one or two-operator scenarios) of the different angular observables in $\Lambda_b \rightarrow \Lambda_c(\rightarrow \Lambda\pi^+)\tau^-\bar{\nu}_\tau$ decays and found correlations among them. We have noted a few one or two-operator scenarios to which some of these observables are sensitive. By measuring these observables, it will be possible to distinguish these effects from one another.

Contents

1	Introduction	1
2	Formalism	2
2.1	Effective Hamiltonian	3
2.2	Decay amplitude and transition matrix elements	3
2.2.1	Hadronic helicity amplitudes	4
2.2.2	Leptonic helicity amplitudes	5
2.3	Angular distribution and Observables	6
3	Form Factor Shape	9
4	Observables: Standard Model Predictions	11
5	Test of New Physics with existing observations: One and two Operator scenario	15
5.1	New Physics analysis: One operator scenario	16
5.2	New physics analysis: Two operators scenario	21
6	Summary	27
7	Acknowledgments	27
8	Appendix	27
8.1	Kinematics in Hadronic rest frame and Hadronic matrix elements	27
8.2	Kinematics in leptonic frame and spinor representation	28
8.2.1	Hadronic Couplings in $\Lambda_c^+ \rightarrow \Lambda\pi^+$	29
8.3	Explicit expression for Angular Observables	29
8.4	BGL Parametrization: Outer function in HQET basis	34
8.5	Transformation: Helicity basis to Transversality basis	35
8.6	Theory Inputs	36

1 Introduction

Over the past few years, the flavour changing charged current (FCCC) decay $b \rightarrow c\ell^-\bar{\nu}$ has been extensively studied in both experimental and theory fronts. So far, most of the studies are focused on the semileptonic decays of B-meson [1]. The semileptonic $B \rightarrow D^{(*)}\ell^-\bar{\nu}$ ($\ell = \mu, e$) decays are useful for the extraction of $|V_{cb}|$ [2–10]. In addition, the ratios of the decay rates which are defined as $R(D^{(*)}) = \Gamma(B \rightarrow D^{(*)}\tau^-\bar{\nu})/\Gamma(B \rightarrow D^{(*)}\ell^-\bar{\nu})$ are potentially sensitive to NP interactions [3, 10–27]. In the SM, these ratios are lepton flavour universality conserving (LFU). These observables are useful for the test of LFU violation, since in a NP scenario these universality might be badly violated. The measurements show discrepancies with the respective SM estimates [1, 28–38], for a recent study see the Refs.[10, 39].

The baryonic decay $\Lambda_b \rightarrow \Lambda_c\ell^-\bar{\nu}$ could provide complementary information. We can extract $|V_{cb}|$ from the measurements of the rates in $\Lambda_b \rightarrow \Lambda_c\ell^-\bar{\nu}$ decays; at the same time, we can extract and test the NP sensitivity of the LFU ratio defined in these modes [39–51]. This process is a spin- $\frac{1}{2}$

to spin- $\frac{1}{2}$ decay process, unlike the spin-0 B meson decay. The Large Hadron Collider (LHC) has produced copious amounts of Λ_b , which provides us with a lot of information on its semileptonic decay. For instance, it has provided the first-ever branching fraction as [52]

$$\mathcal{B}(\Lambda_b \rightarrow \Lambda_c \tau^- \nu_\tau) = (1.50 \pm 0.16 \pm 0.25 \pm 0.23)\%. \quad (1.1)$$

We can obtain more information as more data will come in the next runs. Hence it is an excellent time to study a full 4-body angular distribution for $\Lambda_b \rightarrow \Lambda_c \ell^- \bar{\nu}_\ell$ followed by $\Lambda_c \rightarrow \Lambda \pi$, in both standard model (SM) as well as in the presence of new physics (NP). We can define a considerable number of angular observables which could be predicted and measured. A comparative study of the NP sensitivities of all these observables could be useful in distinguishing the effect of one NP operator from the others. More broadly, this might help to distinguish the effects of different NP models.

The LFUV ratios $R(D^{(*)})$ have provided us with valuable information. However, there are plenty of other observables which are potentially sensitive to new interactions beyond the SM and are correlated with $R(D^{(*)})$ [10, 18]. Therefore, the LFU ratios are insufficient to validate or preclude the BSM contribution to the charge current induced interaction $b \rightarrow c \ell \bar{\nu}$. To validate the effect of NP, one needs to measure all the other observables. Under an effective operator scenario, we may find that LFUV observables are in line with the measurements taken. Recently LHCb has provided LFUV ratio for this baryonic mode $R(\Lambda_c)$ [52] and updated $F_L^{D^*}$ [53]. So, it will be really useful to know what these measurements are implying in terms of New Physics. A full analysis needs to be done incorporating all the NP scenarios and not only taking them one at a time along with SM. The best possible NP scenario will likely be when we take more than one NP operator at a time.

In this article, we have done the angular analysis for $\Lambda_b \rightarrow \Lambda_c^+(\rightarrow \Lambda \pi) \ell^- \bar{\nu}_\ell$ decay and made prediction for SM. Using the measurements on $R(D^{(*)})$, $R(\Lambda_c)$ along with $F_L^{D^*}$ we have done a frequentist analysis with one operator scenario, that can explain the current data simultaneously. We find that it is hard to explain all the data simultaneously if we take the predictions in the NP scenarios at their 1σ uncertainties. And if one tries with two operators at a time the situation improves and specific scenarios can explain all the data simultaneously within 1σ . And if correlation plots between the observables are studied then they will help us to predict the pattern of the measurements and how they can behave for updated measurements.

The paper is structured as follows. In the next section 2, we introduce the formalism used to calculate the amplitude of the decay and discuss the effective Hamiltonian for the four fermions, $b \rightarrow c \tau \nu$, charge current interaction through the introduction of dimension six operators. This section outlines the calculation methodology for angular observables and also includes a review of the other relevant literature for comparison. Next, in section 3, we will discuss the q^2 -shapes of the form factor following the model-independent $z(q^2)$ expansion by the Boyd Grinstein Lebed (BGL) [54] and Bourrely-Caprini-Lellouch (BCL) [55], respectively, and will compare their results. In section 4, we compared our SM results for different observables with both BCL and BGL parameterization in $\ell=\tau, \mu$ decay modes both bin-wise and in the total q^2 region.

Finally, In section 5, we test the NP sensitivity with the exiting results in one(two) parameter scenario at a time and scrutinize the present scenario for all the observables. In the Appendix section we provide the analytical expression for angular observables, and provide predictions for the observables.

2 Formalism

In this section, we define the effective Hamiltonian for a generic NP scenario and then derive the expression for the full angular distribution of the differential decay rate of $\Lambda_b \rightarrow \Lambda_c(\rightarrow \Lambda \pi^+) \ell \bar{\nu}_\ell$.

All the angular coefficients will be expressed in terms of helicity amplitudes which are defined in terms of kinematical variables and hadronic form factors. With explicit expressions for the angular coefficients in hands, we will then proceed and define a set of observables that can be used to study within the standard model and its sensitivity in the presence of the NP.

2.1 Effective Hamiltonian

In the effective theory framework we write the effective Hamiltonian which is obtained after integrating out the heavy degrees of freedom and written in terms of the operators and the corresponding Wilson Coefficients (W.C.) for the semileptonic flavor changing charged current transition $b \rightarrow c\tau^-\bar{\nu}_\tau$ as

$$\mathcal{H}_{eff} = \frac{G_F V_{cb}}{\sqrt{2}} \left\{ \left[(1 + C_{V_1}) \bar{c} \gamma_\mu (1 - \gamma_5) b + C_{V_2} \bar{c} \gamma_\mu (1 + \gamma_5) b \right] \bar{\tau} \gamma^\mu (1 - \gamma_5) \nu_\tau \right. \\ \left. + \left[C_{S_1} \bar{c} (1 + \gamma_5) b + C_{S_2} \bar{c} (1 - \gamma_5) b \right] \bar{\tau} (1 - \gamma_5) \nu_\tau + \left[C_T \bar{c} \sigma^{\mu\nu} (1 - \gamma_5) b \right] \bar{\tau} \sigma_{\mu\nu} (1 - \gamma_5) \nu_\tau + h.c. \right\},$$

where G_F is the Fermi constant, V_{cb} is the Cabibbo-Kobayashi-Maskawa (CKM) matrix element, and we use $\sigma_{\mu\nu} = i[\gamma_\mu, \gamma_\nu]/2$. All the information about short-distance physics and possible new physics effects are contained in the Wilson coefficients which are computed in the perturbation theory as a series in α_s and evaluated at the scale μ using the renormalization group equations. We consider that the above Hamiltonian is written at the m_b energy scale. As standard literature in the absence of New Physics, the C_i 's are zero. Using the quark level effective Hamiltonian for the process to be studied $\Lambda_b(p_{\Lambda_b}) \rightarrow \Lambda_c(p_{\Lambda_c}) + \tau^-(p_\tau) + \bar{\nu}_\tau(p_{\bar{\nu}_\tau})$, where the daughter baryon Λ_c decays to $\Lambda\pi^+$.

2.2 Decay amplitude and transition matrix elements

The larger mass of the b-quark compared to the typical QCD scale ($m_b > \Lambda_{QCD}$) ensures that the perturbative hard part can be factorized from the long-distance hadronic dynamics. After factorizing the short and long-distance pieces, the hadronic matrix elements are expressed in terms of the form factors that carry the non-trivial q^2 dependence, where q generically denotes the momentum transfer for the process. Assuming factorization between the hadronic and leptonic parts, the amplitude of the decay process can be written in terms of the helicity amplitudes $\mathcal{M}_{\lambda_{\Lambda_c}}^{\lambda_\tau}$ as follows:

$$\mathcal{M}_{\lambda_{\Lambda_c}}^{\lambda_\tau} = H_{\lambda_{\Lambda_c}, \lambda=0}^{SP} L^{\lambda_\tau} + \sum_\lambda \eta_\lambda H_{\lambda_{\Lambda_c}, \lambda}^{VA} L_\lambda^{\lambda_\tau} + \sum_{\lambda, \lambda'} \eta_\lambda \eta_{\lambda'} H_{\lambda_{\Lambda_c}, \lambda, \lambda'}^{T, \lambda_{\Lambda_b}} L_{\lambda, \lambda'}^{\lambda_\tau}. \quad (2.1)$$

Here, (λ, λ') indicate the helicity of the virtual vector boson, λ_{Λ_c} and λ_τ are the helicities of the Λ_c baryon and τ lepton, respectively, and $\eta_\lambda = 1$ for $\lambda = t$ and $\eta_\lambda = -1$ for $\lambda = 0, \pm 1$. The semi-leptonic decay $\Lambda_b \rightarrow \Lambda_c \ell \bar{\nu}_\ell$ can be considered as two subsequent 2-body decays, such as the decay $\Lambda_b \rightarrow \Lambda_c W^*$, followed by a subsequent decay of the off-shell W^* to $\ell \nu_\ell$. The off-shell W^* has four helicities, with two angular momentum $J = 0, 1$ in the rest frame of W^* , namely $\lambda = \pm 1, 0$ ($J = 1$) and $\lambda = 0$ ($J = 0$), only the off-shell W^* has time-like polarization. To distinguish the two $\lambda = 0$ states, we adopt the notation $\lambda = 0$ for $J = 1$ and $\lambda = t$ for $J = 0$ ¹. The scalar-type, vector/axial-vector-type, and tensor-type hadronic helicity amplitudes are defined as

$$H_{\lambda_{\Lambda_c}, \lambda=0}^{SP} = H_{\lambda_{\Lambda_c}, \lambda=0}^S + H_{\lambda_{\Lambda_c}, \lambda=0}^P,$$

¹As the Spin-0 component $\lambda=t$ has the property $\bar{\epsilon}_\mu(t) \propto q_\mu$, does not has effects on semileptonic decay in the lepton massless limit.

$$\begin{aligned}
H_{\lambda_{\Lambda_c}, \lambda=0}^S &= (C_{S_1} + C_{S_2}) \langle \Lambda_c | \bar{c} b | \Lambda_b \rangle, \\
H_{\lambda_{\Lambda_c}, \lambda=0}^P &= (C_{S_1} - C_{S_2}) \langle \Lambda_c | \bar{c} \gamma_5 b | \Lambda_b \rangle,
\end{aligned} \tag{2.2}$$

$$\begin{aligned}
H_{\lambda_{\Lambda_c}, \lambda}^{VA} &= H_{\lambda_{\Lambda_c}, \lambda}^V - H_{\lambda_{\Lambda_c}, \lambda}^A, \\
H_{\lambda_{\Lambda_c}, \lambda}^V &= (1 + C_{V_1} + C_{V_2}) \epsilon^{*\mu}(\lambda) \langle \Lambda_c | \bar{c} \gamma_\mu b | \Lambda_b \rangle, \\
H_{\lambda_{\Lambda_c}, \lambda}^A &= (1 + C_{V_1} - C_{V_2}) \epsilon^{*\mu}(\lambda) \langle \Lambda_c | \bar{c} \gamma_\mu \gamma_5 b | \Lambda_b \rangle,
\end{aligned} \tag{2.3}$$

and

$$\begin{aligned}
H_{\lambda_{\Lambda_c}, \lambda, \lambda'}^{T, \lambda_{\Lambda_b}} &= H_{\lambda_{\Lambda_c}, \lambda, \lambda'}^{T1, \lambda_{\Lambda_b}} - H_{\lambda_{\Lambda_c}, \lambda, \lambda'}^{T2, \lambda_{\Lambda_b}}, \\
H_{\lambda_{\Lambda_c}, \lambda, \lambda'}^{T1, \lambda_{\Lambda_b}} &= C_T \epsilon^{*\mu}(\lambda) \epsilon^{*\nu}(\lambda') \langle \Lambda_c | \bar{c} i \sigma_{\mu\nu} b | \Lambda_b \rangle, \\
H_{\lambda_{\Lambda_c}, \lambda, \lambda'}^{T2, \lambda_{\Lambda_b}} &= C_T \epsilon^{*\mu}(\lambda) \epsilon^{*\nu}(\lambda') \langle \Lambda_c | \bar{c} i \sigma_{\mu\nu} \gamma_5 b | \Lambda_b \rangle.
\end{aligned} \tag{2.4}$$

The leptonic amplitudes are defined as

$$\begin{aligned}
L^{\lambda_\tau} &= \langle \tau \bar{\nu}_\tau | \bar{\tau} (1 - \gamma_5) \nu_\tau | 0 \rangle = \bar{u}_\tau (1 - \gamma_5) v_{\bar{\nu}_\tau} \\
L_\lambda^{\lambda_\tau} &= \epsilon^\mu(\lambda) \langle \tau \bar{\nu}_\tau | \bar{\tau} \gamma_\mu (1 - \gamma_5) \nu_\tau | 0 \rangle = \epsilon^\mu(\lambda) \bar{u}_\tau \gamma_\mu (1 - \gamma_5) v_{\bar{\nu}_\tau} \\
L_{\lambda, \lambda'}^{\lambda_\tau} &= -i \epsilon^\mu(\lambda) \epsilon^\nu(\lambda') \langle \tau \bar{\nu}_\tau | \bar{\tau} \sigma_{\mu\nu} (1 - \gamma_5) \nu_\tau | 0 \rangle = -i \epsilon^\mu(\lambda) \epsilon^\nu(\lambda') \bar{u}_\tau \sigma_{\mu\nu} (1 - \gamma_5) v_{\bar{\nu}_\tau}.
\end{aligned} \tag{2.5}$$

Above, ϵ^μ are the polarization vectors of the virtual vector boson. The explicit expressions for the hadronic and leptonic helicity amplitudes are presented in the following.

So finally the decay rate for $\Lambda_b \rightarrow \Lambda_c (\rightarrow \Lambda \pi) \tau \bar{\nu}_\tau$ can be written by taking into account the phase factor as follows:

$$\frac{d\Gamma}{dq^2} = N \sum_{\lambda_{\Lambda_c}} \sum_{\lambda_\tau} |\mathcal{M}_{\lambda_{\Lambda_c}}^{\lambda_\tau} \mathcal{A}_{\lambda_{\Lambda_c}}^{\lambda_{\Lambda_b}}|^2 \tag{2.6}$$

with $N = \frac{G_F^2 |V_{cb}|^2}{1536\pi^3} (1 - \frac{m_\tau^2}{q^2}) \frac{\sqrt{Q_+ Q_-}}{m_{\Lambda_b}^3} \mathcal{B}(\Lambda_c \rightarrow \Lambda \pi)$ Where, $\mathcal{B}(\Lambda_c \rightarrow \Lambda \pi) = (1.29 \pm 0.05)\%$ [56]

2.2.1 Hadronic helicity amplitudes

In the following, only the non-vanishing helicity amplitudes are given. The scalar and pseudo-scalar helicity amplitudes associated with the new physics scalar and pseudo-scalar interactions are

$$H_{1/2,0}^{SP} = f_0 (C_{S_1} + C_{S_2}) \frac{\sqrt{Q_+}}{m_b - m_c} (m_{\Lambda_b} - m_{\Lambda_c}) - g_0 (C_{S_1} - C_{S_2}) \frac{\sqrt{Q_-}}{m_b + m_c} (m_{\Lambda_b} + m_{\Lambda_c}), \tag{2.7}$$

$$H_{-1/2,0}^{SP} = f_0 (C_{S_1} + C_{S_2}) \frac{\sqrt{Q_+}}{m_b - m_c} (m_{\Lambda_b} - m_{\Lambda_c}) + g_0 (C_{S_1} - C_{S_2}) \frac{\sqrt{Q_-}}{m_b + m_c} (m_{\Lambda_b} + m_{\Lambda_c}). \tag{2.8}$$

The parity-related amplitudes are

$$\begin{aligned}
H_{\lambda_{\Lambda_c}, \lambda_{NP}}^S &= H_{-\lambda_{\Lambda_c}, -\lambda_{NP}}^S, \\
H_{\lambda_{\Lambda_c}, \lambda_{NP}}^P &= -H_{-\lambda_{\Lambda_c}, -\lambda_{NP}}^P.
\end{aligned} \tag{2.9}$$

For the vector and axial-vector helicity amplitudes, we find

$$H_{1/2,0}^{VA} = f_+(1 + C_{V_1} + C_{V_2}) \frac{\sqrt{Q_-}}{\sqrt{q^2}} (m_{\Lambda_b} + m_{\Lambda_c}) - g_+(1 + C_{V_1} - C_{V_2}) \frac{\sqrt{Q_+}}{\sqrt{q^2}} (m_{\Lambda_b} - m_{\Lambda_c}), \tag{2.10}$$

$$H_{1/2,+1}^{VA} = -f_\perp (1 + C_{V_1} + C_{V_2}) \sqrt{2Q_-} + g_\perp (1 + C_{V_1} - C_{V_2}) \sqrt{2Q_+}, \tag{2.11}$$

$$H_{1/2,t}^{VA} = f_0(1 + C_{V_1} + C_{V_2}) \frac{\sqrt{Q_+}}{\sqrt{q^2}} (m_{\Lambda_b} - m_{\Lambda_c}) - g_0(1 + C_{V_1} - C_{V_2}) \frac{\sqrt{Q_-}}{\sqrt{q^2}} (m_{\Lambda_b} + m_{\Lambda_c}), \quad (2.12)$$

$$H_{-1/2,0}^{VA} = f_+(1 + C_{V_1} + C_{V_2}) \frac{\sqrt{Q_-}}{\sqrt{q^2}} (m_{\Lambda_b} + m_{\Lambda_c}) + g_+(1 + C_{V_1} - C_{V_2}) \frac{\sqrt{Q_+}}{\sqrt{q^2}} (m_{\Lambda_b} - m_{\Lambda_c}), \quad (2.13)$$

$$H_{-1/2,-1}^{VA} = -f_\perp(1 + C_{V_1} + C_{V_2}) \sqrt{2Q_-} - g_\perp(1 + C_{V_1} - C_{V_2}) \sqrt{2Q_+}, \quad (2.14)$$

$$H_{-1/2,t}^{VA} = f_0(1 + C_{V_1} + C_{V_2}) \frac{\sqrt{Q_+}}{\sqrt{q^2}} (m_{\Lambda_b} - m_{\Lambda_c}) + g_0(1 + C_{V_1} - C_{V_2}) \frac{\sqrt{Q_-}}{\sqrt{q^2}} (m_{\Lambda_b} + m_{\Lambda_c}). \quad (2.15)$$

We also have the relations $H_{\lambda_{\Lambda_c}, \lambda_w}^{VA} = H_{\lambda_{\Lambda_c}, \lambda_w}^V - H_{\lambda_{\Lambda_c}, \lambda_w}^A$ where

$$\begin{aligned} H_{\lambda_{\Lambda_c}, \lambda_w}^V &= H_{-\lambda_{\Lambda_c}, -\lambda_w}^V, \\ H_{\lambda_{\Lambda_c}, \lambda_w}^A &= -H_{-\lambda_{\Lambda_c}, -\lambda_w}^A. \end{aligned} \quad (2.16)$$

The tensor helicity amplitudes are

$$H_{-1/2,t,0}^{T,-1/2} = -C_T \left[-h_+ \sqrt{Q_-} + \tilde{h}_+ \sqrt{Q_+} \right], \quad (2.17)$$

$$H_{+1/2,t,0}^{T,+1/2} = C_T \left[h_+ \sqrt{Q_-} + \tilde{h}_+ \sqrt{Q_+} \right], \quad (2.18)$$

$$H_{+1/2,t,+1}^{T,-1/2} = -C_T \frac{\sqrt{2}}{\sqrt{q^2}} \left[h_\perp (m_{\Lambda_b} + m_{\Lambda_c}) \sqrt{Q_-} + \tilde{h}_\perp (m_{\Lambda_b} - m_{\Lambda_c}) \sqrt{Q_+} \right], \quad (2.19)$$

$$H_{-1/2,t,-1}^{T,+1/2} = -C_T \frac{\sqrt{2}}{\sqrt{q^2}} \left[h_\perp (m_{\Lambda_b} + m_{\Lambda_c}) \sqrt{Q_-} - \tilde{h}_\perp (m_{\Lambda_b} - m_{\Lambda_c}) \sqrt{Q_+} \right], \quad (2.20)$$

$$H_{+1/2,0,+1}^{T,-1/2} = -C_T \frac{\sqrt{2}}{\sqrt{q^2}} \left[h_\perp (m_{\Lambda_b} + m_{\Lambda_c}) \sqrt{Q_-} + \tilde{h}_\perp (m_{\Lambda_b} - m_{\Lambda_c}) \sqrt{Q_+} \right], \quad (2.21)$$

$$H_{-1/2,0,-1}^{T,+1/2} = C_T \frac{\sqrt{2}}{\sqrt{q^2}} \left[h_\perp (m_{\Lambda_b} + m_{\Lambda_c}) \sqrt{Q_-} - \tilde{h}_\perp (m_{\Lambda_b} - m_{\Lambda_c}) \sqrt{Q_+} \right], \quad (2.22)$$

$$H_{+1/2,+1,-1}^{T,+1/2} = -C_T \left[h_+ \sqrt{Q_-} + \tilde{h}_+ \sqrt{Q_+} \right], \quad (2.23)$$

$$H_{-1/2,+1,-1}^{T,-1/2} = -C_T \left[h_+ \sqrt{Q_-} - \tilde{h}_+ \sqrt{Q_+} \right]. \quad (2.24)$$

The other non-vanishing helicity amplitudes of tensor type are related to the above by

$$H_{\lambda_{\Lambda_c}, \lambda, \lambda'}^{T, \lambda_{\Lambda_b}} = -H_{\lambda_{\Lambda_c}, \lambda', \lambda}^{T, \lambda_{\Lambda_b}}. \quad (2.25)$$

2.2.2 Leptonic helicity amplitudes

In the calculation of the lepton helicity amplitudes, we work in the rest frame of the virtual vector boson, the $\tau\bar{\nu}_\tau$ dilepton rest frame. We define the angle θ_τ as the angle between the three-momenta of the τ and the Λ_c in this frame.

In the following, we define $v = \sqrt{1 - \frac{m_\tau^2}{q^2}}$. The scalar and pseudo-scalar leptonic helicity amplitudes are

$$L^{+1/2} = 2\sqrt{q^2}v, \quad (2.26)$$

$$L^{-1/2} = 0, \quad (2.27)$$

the vector and axial-vector amplitudes are (we got)

$$L_{\pm 1}^{+1/2} = \pm \sqrt{2} m_\tau v \sin(\theta_\tau), \quad (2.28)$$

$$L_0^{+1/2} = -2 m_\tau v \cos(\theta_\tau), \quad (2.29)$$

$$L_t^{+1/2} = 2 m_\tau v, \quad (2.30)$$

$$L_{\pm 1}^{-1/2} = \sqrt{2} q^2 v (1 \pm \cos(\theta_\tau)), \quad (2.31)$$

$$L_0^{-1/2} = 2 \sqrt{q^2} v \sin(\theta_\tau), \quad (2.32)$$

$$L_t^{-1/2} = 0, \quad (2.33)$$

and the tensor amplitudes are

$$L_{0,\pm 1}^{+1/2} = -\sqrt{2} q^2 v \sin(\theta_\tau), \quad (2.34)$$

$$L_{\pm 1,t}^{+1/2} = \mp \sqrt{2} q^2 v \sin(\theta_\tau), \quad (2.35)$$

$$L_{t,0}^{+1/2} = L_{+1,-1}^{+1/2} = -2 \sqrt{q^2} v \cos(\theta_\tau), \quad (2.36)$$

$$L_{0,\pm 1}^{-1/2} = \mp \sqrt{2} m_\tau v (1 \pm \cos(\theta_\tau)), \quad (2.37)$$

$$L_{\pm 1,t}^{-1/2} = -\sqrt{2} m_\tau v (1 \pm \cos(\theta_\tau)), \quad (2.38)$$

$$L_{t,0}^{-1/2} = L_{+1,-1}^{-1/2} = 2 m_\tau v \sin(\theta_\tau). \quad (2.39)$$

Here we have the relation

$$L_{\lambda,\lambda'}^{\lambda_\tau} = -L_{\lambda',\lambda}^{\lambda_\tau}. \quad (2.40)$$

2.3 Angular distribution and Observables

The four-fold differential decay rate of $\Lambda_b \rightarrow \Lambda_c^+ (\rightarrow \Lambda \pi^+) \tau \bar{\nu}_\tau$ decay, with a unpolarized Λ_b baryon, is fully parameterized in terms of q^2 and the three angles as introduced in fig. 1.

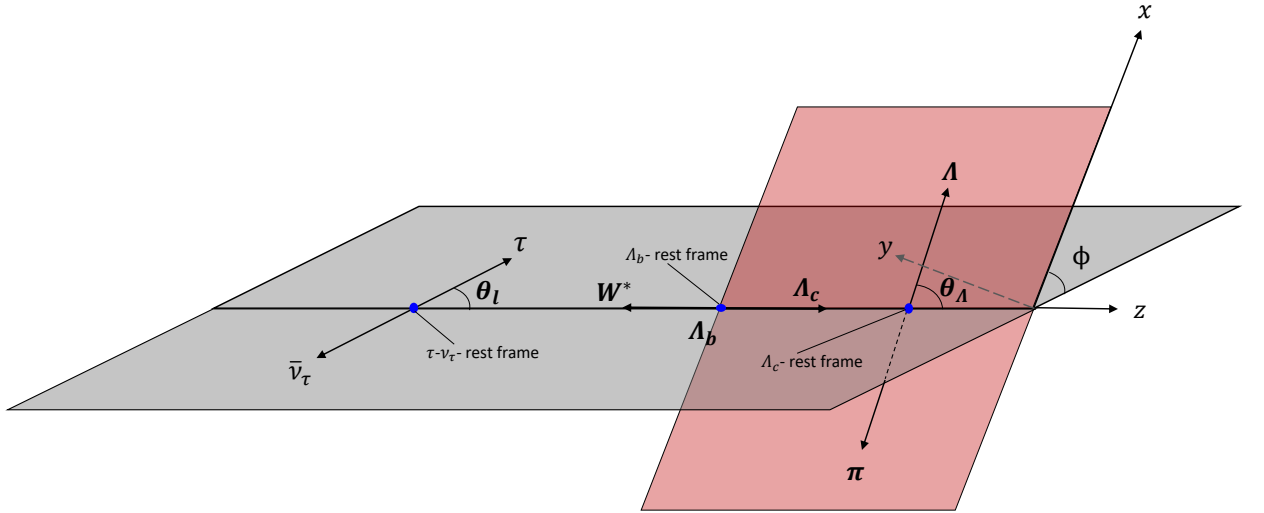


Figure 1: The schematic diagram of the 4-body $\Lambda_b \rightarrow \Lambda_c (\rightarrow \Lambda \pi^+) \ell \bar{\nu}_\ell$ decay.

- θ_ℓ : The angle between the leptons and the direction to the Λ_c baryon in the virtual W-boson rest frame.
- θ_Λ : The angle between the Λ baryon and direction of the Λ_c baryon in the Λ_c rest frame.
- ϕ : The azimuthal angle between the two decay planes spanned by $W^*-\ell$ and $\Lambda_c-\Lambda$ system in the Λ_b rest frame.

The measurable 4-fold angular decay distribution can then be written as

$$\frac{d\Gamma}{dq^2 d\cos\theta_\ell d\cos\theta_\Lambda d\phi} = \frac{3}{8\pi} K(q^2, \cos\theta_\ell, \cos\theta_\Lambda, \phi) \quad (2.41)$$

where the angular distribution $K(q^2, \cos\theta_\ell, \cos\theta_\Lambda, \phi)$ depends only on the di-lepton invariant mass square, q^2 , and contains the hadronic information which in turn is expressed in terms of the hadronic helicity amplitude, parametrized by WC's and baryonic form factors, and can be expressed as follows:

$$\begin{aligned} K(q^2, \cos\theta_\ell, \cos\theta_\Lambda, \phi) = & (K_{1ss} \sin^2\theta_\ell + K_{1cc} \cos^2\theta_\ell + K_{1c} \cos\theta_\ell) \\ & + (K_{2ss} \sin^2\theta_\ell + K_{2cc} \cos^2\theta_\ell + K_{2c} \cos\theta_\ell) \cos\theta_\Lambda \\ & + (K_{3sc} \sin\theta_\ell \cos\theta_\ell + K_{3s} \sin\theta_\ell) \sin\theta_\Lambda \cos\phi \\ & + (K_{4sc} \sin\theta_\ell \cos\theta_\ell + K_{4s} \sin\theta_\ell) \sin\theta_\Lambda \sin\phi. \end{aligned} \quad (2.42)$$

The expressions for the K_i 's are written in terms of helicity amplitudes and are given in Appendix. 8.3. ²

By integrating over the lepton-side angle θ_ℓ and the azimuthal angle ϕ we can obtain the two-fold differential decay rate as follows-

$$\frac{d^2\Gamma}{dq^2 d\cos\theta_\Lambda} = \frac{1}{2} \frac{d\Gamma}{dq^2} (1 + \alpha_\Lambda P_{\Lambda_c}(q^2) \cos\theta_\Lambda) \quad (2.43)$$

Here, $P_{\Lambda_c}(q^2)$ represents the Λ_c spin polarization, which defined as

$$P_{\Lambda_c}(q^2) = \frac{d\Gamma^{\lambda_{\Lambda_c}=1/2}/dq^2 - d\Gamma^{\lambda_{\Lambda_c}=-1/2}/dq^2}{d\Gamma/dq^2}. \quad (2.44)$$

Here, $\frac{d\Gamma^{\lambda_{\Lambda_c}=\pm 1/2}}{dq^2}$ are the differential decay rates for the polarized intermediate state Λ_c baryon given in Appendix. 8.3.

Further integrating over the hadronic angle θ_Λ , we can obtain the following differential decay rate depending only on q^2 .

$$\frac{d\Gamma}{dq^2} = 2K_{1ss} + K_{1cc} \quad (2.45)$$

All the angular asymmetries are defined and in experiments also they are measured by normalised the decay rate, so we define

$$\hat{K}_i = \frac{K_i}{2K_{1ss} + K_{1cc}} \quad (2.46)$$

Also, we can construct another asymmetric observable associated with the lepton polarization λ_ℓ , in particular, the τ -polarization asymmetry:

$$P_\tau^{(\Lambda_c)}(q^2) = \frac{d\Gamma^{\lambda_\tau=1/2}/dq^2 - d\Gamma^{\lambda_\tau=-1/2}/dq^2}{d\Gamma/dq^2}. \quad (2.47)$$

²With the given spinor and W^* polarization vector, define in ref [43], we could not find the given leptonic helicity amplitudes in ref [43].

For explicit expression of $\frac{d\Gamma^{\lambda\tau=\pm 1/2}}{dq^2}$, one can see from Appendix. 8.3. Also, we obtain the convexity parameter $C_F^\ell(q^2)$ defined by

$$C_F^\ell(q^2) = \frac{1}{d\Gamma/dq^2} \left(\frac{d}{d(\cos\theta_l)} \right)^2 \left(\frac{d^2\Gamma}{dq^2 d\cos\theta_l} \right). \quad (2.48)$$

The detail expression for C_F^ℓ are given in Appendix. 8.3.

Among the other important observables, the forward-backward asymmetry concerning the leptonic scattering angle, normalized to the differential rate, is defined as

$$A_{\text{FB}}^\ell = \frac{3}{2} \frac{K_{1c}}{2K_{1ss} + K_{1cc}} \quad (2.49)$$

which can be extracted from eqn. 2.42 as

$$A_{\text{FB}}^\ell = \frac{\int_0^{2\phi} d\phi \int_0^1 d\cos\theta_\Lambda [\int_0^1 - \int_{-1}^0] d\cos\theta_\ell K(q^2, \cos\theta_\ell, \cos\theta_\Lambda, \phi)}{\int_0^{2\phi} d\phi \int_0^1 d\cos\theta_\Lambda \int_{-1}^1 d\cos\theta_\ell K(q^2, \cos\theta_\ell, \cos\theta_\Lambda, \phi)} \quad (2.50)$$

The analogous asymmetry for the baryonic scattering angle reads

$$A_{\text{FB}}^{\Lambda_c} = \frac{1}{2} \frac{2K_{2ss} + K_{2cc}}{2K_{1ss} + K_{1cc}}. \quad (2.51)$$

Using eqn. 2.42 we can define the above asymmetry as

$$A_{\text{FB}}^{\Lambda_c} = \frac{\int_0^{2\phi} d\phi \int_0^1 d\cos\theta_\ell [\int_0^1 - \int_{-1}^0] d\cos\theta_\Lambda K(q^2, \cos\theta_\ell, \cos\theta_\Lambda, \phi)}{\int_0^{2\phi} d\phi \int_0^1 d\cos\theta_\Lambda \int_{-1}^1 d\cos\theta_\ell K(q^2, \cos\theta_\ell, \cos\theta_\Lambda, \phi)} \quad (2.52)$$

For $\Lambda_b \rightarrow \Lambda_c (\rightarrow \Lambda\pi^+) \ell^- \bar{\nu}$ decays, one could also define a combined forward-backward asymmetry defined by

$$A_{\text{FB}}^{\Lambda_c\ell} = \frac{3}{4} \frac{K_{2c}}{2K_{1ss} + K_{1cc}} \quad (2.53)$$

and can be extracted from eqn. 2.42 following the integrations as given below

$$A_{\text{FB}}^{\Lambda_c\ell} = \frac{\int_0^{2\phi} d\phi [\int_0^1 - \int_{-1}^0] d\cos\theta_\Lambda [\int_0^1 - \int_{-1}^0] d\cos\theta_\ell K(q^2, \cos\theta_\ell, \cos\theta_\Lambda, \phi)}{\int_0^{2\phi} d\phi \int_0^1 d\cos\theta_\Lambda \int_{-1}^1 d\cos\theta_\ell K(q^2, \cos\theta_\ell, \cos\theta_\Lambda, \phi)} \quad (2.54)$$

After reviewing the other literature, we have summarized our findings as follows:

- We have found that our results are in complete agreement with the result of [43] regarding the $\frac{d\Gamma}{dq^2}$, two-fold decay distribution in the presence of all scalar, vector, tensor dim-6 operator.
- The ref. [49] taken NP operators in their angular distribution in the form of transversity amplitudes. Assuming that they have taken the notation as written in Appendix 8.5, it matches with the $\frac{d\Gamma}{dq^2}$ of our calculation and as we have matched with [43], it matches with [43]. For each angular observable, we have a factor of 4 extra which gives the same value after normalizing.
- For ref [42] we get an extra factor of 4 only for the tensor amplitudes though we have taken the same notation for tensor Hamiltonian. So all the terms with interference with tensor has extra 4 and the $|C_T^2|$ terms has extra 16.

- On the other hand, our findings differ from the results of ref. [41], which only consider the cascade decay in the presence of scalar and vector dimension-six operators. Our research result aligns with the findings of the literature ref. [49]. We have observed interference terms of the type $V \times S$ and $A \times P$ in our angular observables K_{3s} and K_{4s} , which are absent from the corresponding term C^{int_4} of ref. [41]. We have also found a lack of an overall multiplicative factor $\mathcal{B}(\Lambda_c \rightarrow \Lambda\pi)$. Furthermore, we have achieved agreement only by redefining the angles $\theta_\tau \rightarrow \pi - \theta$, $\theta_{\Lambda_c} \rightarrow \theta_s$, and $\phi \rightarrow -\chi$.

3 Form Factor Shape

We have noted in the last section that the helicity or the transversity amplitudes of the hadronic current are dependent on the non-perturbative form factors and their q^2 shapes. Hence, to get the shape of the decay rate distribution, one needs to know the shape of the corresponding form factors in the whole q^2 region. The lattice simulation in the ref. [40] uses the BCL parametrization to obtain the shapes of the form factors. We use their fit results for the BCL coefficients to obtain the shapes of the form factors. Using these shapes we have obtained the decay rate distributions and predicted many other related observables which we will discuss in the following sections.

$\mathbf{0}^-/\text{GeV}$	$\mathbf{0}^+/\text{GeV}$	$\mathbf{1}^-/\text{GeV}$	$\mathbf{1}^+/\text{GeV}$
6.2749	6.6925	6.3290	6.7305
6.8710	7.1045	6.8975	6.7385
		7.0065	7.1355
			7.1435

Table 1: Pole masses used in the BGL parametrization.

observables	Values
$\tilde{\chi}_{0-}^L(0)$	19.412×10^{-3}
$\chi_{0+}^L(0)$	6.204×10^{-3}
$\chi_{1-}^T(0)$	$5.131 \times 10^{-4} \text{ GeV}^{-2}$
$\chi_{1+}^T(0)$	$3.894 \times 10^{-4} \text{ GeV}^{-2}$

Table 2: $\chi^i, \tilde{\chi}$ values that are entering into the form factor through the outer function $\phi(t)$.

In addition, we have created synthetic data points for the form factors at a few q^2 values using the fit results and the correlations given in ref. [40]. Using these synthetic data points we have extracted the coefficients of the $z(q^2)$ expansion of the form factors using BGL parametrization. Following the BGL, we can obtain the shape of the form factors as given below

$$F_i(q^2) = \frac{1}{P_i(q^2)\phi_i(q^2, t_0)} \sum_{j=0}^N a_j^i z^j. \quad (3.1)$$

The conformal map from q^2 to $z \equiv z[q^2; t_0]$ is given by :

$$z(q^2, t_0) = \frac{\sqrt{t_+ - q^2} - \sqrt{t_+ - t_0}}{\sqrt{t_+ - q^2} + \sqrt{t_+ - t_0}}, \quad (3.2)$$

where $t_{\pm} \equiv (m_{\Lambda_b} \pm m_F)^2$ and $t_0 \equiv t_+(1 - \sqrt{1 - t_-/t_+})$. F refers to the final state meson. t_0 is a free parameter that governs the size of z in the semileptonic phase space. The coefficients a_j^i follow weak as well as strong unitarity constraints [54].

$$\sum_{j=0}^2 (a_j^{H_V})^2 + (a_j^{F_1})^2 \leq 1, \quad \sum_{j=0}^2 (a_j^{H_A})^2 + (a_j^{G_1})^2 \leq 1, \quad \text{and,} \quad \sum_{j=0}^2 (a_j^{F_0})^2 \leq 1, \quad \sum_{j=0}^2 (a_j^{G_0})^2 \leq 1. \quad (3.3)$$

In eqn. 3.1, the variable z is also related to the recoil variable w ($w = v_{\Lambda_b} \cdot v_F$ with v_{Λ_b} and v_F being the four-velocities of the Λ_b and the final state mesons respectively) as

$$z = \frac{\sqrt{w+1} - \sqrt{2}}{\sqrt{w+1} + \sqrt{2}}, \quad (3.4)$$

where w is related to the momentum transferred to the dilepton system (q^2) as $q^2 = m_{\Lambda_b}^2 + m_F^2 - 2m_{\Lambda_b}m_F w$. The Blaschke factor $P_i(q^2)$ accounts for the poles in $f_i(q^2)$ for the subthreshold resonances with the same spin-parity as the current defining the form factors. Mathematically, the $P_i(q^2)$ is defined as

$$P_i(q^2) = \prod_p z[q^2; t_p], \quad (3.5)$$

where for a single pole

$$z[q^2; t_p] = \frac{z - z_p}{1 - z z_p}, \quad \text{with } z_p \equiv z[t_p; t_0]. \quad (3.6)$$

The role of the $P_i(q^2)$ is to eliminate the poles in $f_i(q^2)$ at the resonance masses below the threshold. Following eqn. 3.2, we will get

$$z_p = \frac{\sqrt{(m_{\Lambda_b} + m_F)^2 - m_P^2} - \sqrt{4m_{\Lambda_b}m_F}}{\sqrt{(m_{\Lambda_b} + m_F)^2 - m_P^2} + \sqrt{4m_{\Lambda_b}m_F}}. \quad (3.7)$$

Here, m_P denotes the pole masses and the relevant inputs with appropriate spin are presented in table 1. The detailed calculation of the outer functions $\phi_i(q^2; t_0)$ are available in [54], which we have presented in eqns. 8.31. The numerical inputs for the perturbatively calculable χ -functions which appear in the outer functions are shown in table 2, which we have extracted using the results in [54].

We have mentioned above that the q^2 shape of the vector, axial, and tensor form factors in $\Lambda_b \rightarrow \Lambda_c$ decay [40] using the BCL parametrization. They generated the simulated data to do a fit to the respective form factor and presented their BCL parameter fit results and their correlations. The details of the relevant inputs used in the BCL parameterization can be seen from the ref. [40] which have been incorporated into our analysis. Using their fit results we have generated the synthetic data points for the form factors at values $q^2 = 0, 5, 10 \text{ GeV}^2$, which we have shown in table 3. Using these data points along with the respective correlations, we have extracted the BGL coefficients using the χ^2 minimization procedure. Note that in the BGL expansion, we have presented our results considering terms up to order $j = 2$. We have checked that the current lattice inputs are insensitive to the higher order ($j > 2$) BGL coefficients. The χ^2 function which is the negative of the logarithm of the likelihood function is defined as

$$\chi^2 = \sum_{i,j} (O_i^{\text{theory}} - O_i^{\text{lattice}}) V_{ij}^{-1} (O_j^{\text{theory}} - O_j^{\text{lattice}}). \quad (3.8)$$

Form Factor	q^2 (GeV ²)		
	0	5	10
f_+	0.431(49)	0.669(34)	1.020(32)
f_0	0.431(49)	0.625(32)	0.902(25)
f_\perp	0.588(91)	0.904(58)	1.377(49)
g_+	0.387(37)	0.572(25)	0.832(21)
g_0	0.387(37)	0.607(28)	0.936(30)
g_\perp	0.372(39)	0.561(26)	0.830(21)

Table 3: Synthetic data for the $\Lambda_b \rightarrow \Lambda_c$ form factors generated using lattice information, BCL parameter along with their correlations.

BGL Coeff.	Fit Results	BGL Coeff.	Fit Results
$a_{F_0}^0$	0.0482(15)	$a_{F_1}^0$	0.0403(16)
$a_{F_0}^1$	-0.490(90)	$a_{F_1}^1$	-0.434(95)
$a_{G_0}^0$	0.0673(23)	$a_{F_1}^2$	0.83(107)
$a_{G_0}^1$	-0.74(13)	$a_{H_V}^0$	0.0111(4)
$a_{G_1}^0$	0.01614(43)	$a_{H_V}^1$	-0.131(21)
$a_{G_1}^1$	-0.149(24)	$a_{H_V}^2$	0.33(30)
$a_{G_1}^2$	0.094(340)		
$a_{H_A}^1$	-0.0243(34)		
$a_{H_A}^2$	0.029(34)		
DOF	2	p-Value	0.578

Table 4: Fit results for the BGL coefficients a_i^n corresponding to the $\Lambda_b \rightarrow \Lambda_c$ transition form factors. We took $n = 2$ for form factor BGL parameterization, exploiting the QCD constraints at zero and large recoil.

Here, O_i^{theory} s are the expressions of the form factors at $q^2 = 0, 5, \text{ and } 10 \text{ GeV}^2$, respectively, parametrized in terms of the BGL coefficients. The $O_i^{lattices}$ s are the respective inputs on the form factors given in table 3 and V_{ij} is the covariance matrix comprising the information of the correlation and error value of the corresponding lattice inputs. Our fit results for the BGL coefficients are shown in table 4. Note that we have obtained a p-value of the fit around 58%, which could be considered as a good fit. Using these fit results, we are able to reproduce the respective shapes of the all the form factors obtained in [40] which we have not shown here. All the fits and subsequent analyses have been carried out using a Mathematica[®] package[57].

4 Observables: Standard Model Predictions

Using the shapes of the form factors obtained in BCL and BGL parametrizations, respectively, we have obtained the q^2 distributions of the decay rates and the other angular observables. In fig. 2, we have shown the respective q^2 distributions for the final state lepton $\ell = \mu$ and τ . The bands indicate the respective 1σ error bars. In both the parametrizations we have obtained identical results, hence, we have shown these plots only for the BGL parametrization. Also, we have predicted the q^2 integrated decay rates and the angular observables in the SM. Here, we have done a comparison of the results in both the parametrization which will help us to check whether or not

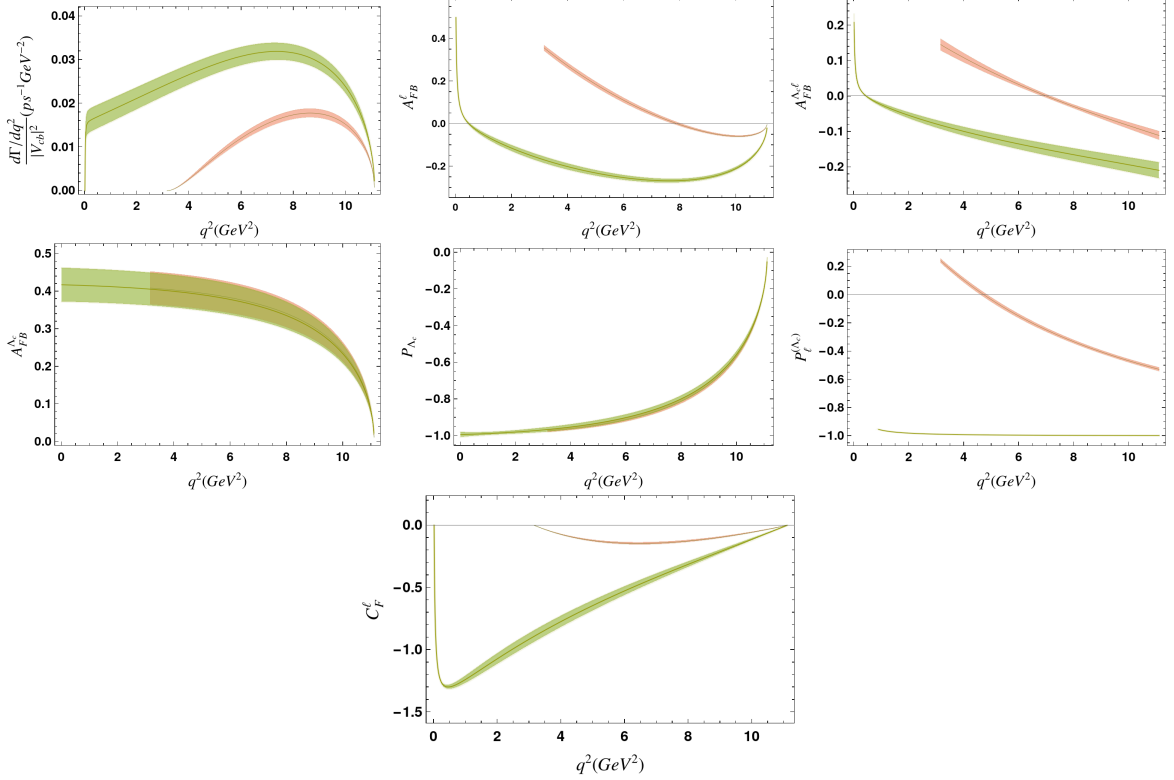


Figure 2: Our estimates for the differential decay distribution, forward-backward asymmetry, and polarization observables for lepton, as well as baryon and convexity observables respectively within BGL parameterization for a tauon (brown) and a muon (green) in the final state in the SM, and the color bands corresponds to the 68% confidence interval.

the predictions are independent of the different methods of obtaining the q^2 shapes. The numerical estimates in different small q^2 -bins are presented in table 5 for the final state with a muon and in table 6 for a τ in the final state, respectively. Note that we have presented the q^2 integrated values in small bins, also, we have shown the SM predictions integrated in the full q^2 region. We have shown the SM predictions for the rates $\Gamma(\Lambda_b \rightarrow \Lambda_c^+(\rightarrow \Lambda\pi)\ell^-\bar{\nu}_\ell)$ normalized by the CKM element $|V_{cb}|^2$. Depending on the value of $|V_{cb}|$ one will be able to extract the respective number. Following are few comments based on the q^2 distributions or the predictions of the observables in small q^2 bins.

- $\frac{d\Gamma(q^2)}{dq^2}$: The q^2 dependence of the differential decay rate for $\Lambda_b \rightarrow \Lambda_c^+(\rightarrow \Lambda\pi)\ell^-\bar{\nu}_\ell$ decay has shown in fig. 2 within the standard model. For the muon mode, the differential ratio shows a step-like behavior when $q^2 = m_\mu^2$. And at the zero recoil, $q_{\text{max}}^2 = (m_{\Lambda_b} - m_{\Lambda_c})^2$, the differential decay rate for both the modes, μ and τ converge to zero because of the unavailability of the phase-space.
- $A_{FB}^\ell(q^2)$: At the zero recoil, the forward-backward asymmetries of the leptonic side, A_{FB}^ℓ , approaches to zero for both the leptonic modes μ and τ . However, at $q^2 = m_\ell^2$, the asymmetry takes the value

$$A_{FB}^\mu(m_\mu^2) = 0.4994(1), \quad A_{FB}^\tau(m_\tau^2) = 0.356(13). \quad (4.1)$$

Furthermore, A_{FB}^ℓ is positive for most of the kinematic range and zero crossing occurs at $q_0^2 = 7.918(166)\text{GeV}^2$, has a small negative value at the high q^2 region. Whereas, A_{FB}^μ , is

Obs.	Parametrization	q^2 Bin (in GeV^2)					
		q_{\min}^2-3	$3-5$	$5-7$	$7-9$	$9-q_{\max}^2$	$q_{\min}^2-q_{\max}^2$
$\langle \frac{\Gamma}{ \vec{v}_c \cdot \vec{v}_\pi} \rangle$	BCL	0.059(8)	0.053(5)	0.061(4)	0.063(4)	0.046(3)	0.281(20)
	BGL	0.059(8)	0.053(5)	0.061(4)	0.062(4)	0.045(3)	0.281(20)
$\langle A_{FB}^\mu \rangle$	BCL	0.149(8)	-0.199(15)	-0.251(11)	-0.264(9)	-0.189(7)	tab. 7
	BGL	0.149(7)	-0.199(15)	-0.251(11)	-0.264(9)	-0.189(7)	-
$\langle A_{FB}^{\Lambda_c \mu} \rangle$	BCL	0.060(7)	-0.098(12)	-0.135(15)	-0.165(18)	-0.195(21)	tab. 7
	BGL	0.060(7)	-0.098(12)	-0.135(15)	-0.165(18)	-0.195(21)	-
$\langle A_{FB}^{\Lambda_c} \rangle$	BCL	0.416(45)	0.400(43)	0.377(41)	0.333(36)	0.212(24)	0.387(42)
	BGL	0.416(45)	0.400(43)	0.377(41)	0.333(36)	0.212(23)	0.387(42)
$\langle P_{\Lambda_c} \rangle$	BCL	-0.982(8)	-0.950(14)	-0.896(17)	-0.789(18)	-0.495(15)	-0.757(17)
	BGL	-0.982(8)	-0.950(14)	-0.897(17)	-0.790(18)	-0.495(15)	-0.758(17)
$\langle P_\mu^{(\Lambda_c)} \rangle$	BCL	-0.937(3)	-0.9914(2)	-0.9948(2)	-0.9965(1)	-0.9975(1)	-0.988(1)
	BGL	-0.937(2)	-0.9913(3)	-0.9948(2)	-0.9965(1)	-0.9975(1)	-0.988(1)
$\langle C_F^\ell(q^2) \rangle$	BCL	-0.854(10)	-0.780(45)	-0.529(36)	-0.313(23)	-0.107(9)	-0.711(24)
	BGL	-0.854(10)	-0.779(45)	-0.529(35)	-0.313(22)	-0.107(8)	-0.711(24)

Table 5: Bin-wise observables prediction for $\Lambda_b \rightarrow \Lambda_c(\rightarrow \Lambda\pi)\mu\bar{\nu}_\mu$ mode.

negative for all of the kinematic range and became positive at large recoil and zero crossing occurs at $\mathbf{q_0^2 = 0.481(45) GeV^2}$.

- $A_{FB}^{\Lambda_c}(q^2)$: Due to the absence of any threshold effects with respect to the dilepton invariant mass square, q^2 , the two bands for the hadronic forward-backward asymmetry is virtually indistinguishable. Hence any deviation from the above would exhibit large NP effects which we will discuss later.
- $A_{FB}^{\Lambda_c \ell}(q^2)$: For both the leptonic final states these asymmetries have zero crossings. For taonic mode, the zero crossing occur at $\mathbf{q_0^2 = 7.011(165) GeV^2}$ where as $A_{FB}^{\Lambda_c \mu}$ has a negative value for the most of the kinematic range and zero crossing occurs at $\mathbf{q_0^2 = 0.454(39) GeV^2}$.
- $P_{\Lambda_c}(q^2)$: We could see that the q^2 distributions of the Λ_c polarization asymmetries for both the leptonic channels overlap with each other. This longitudinal hadronic polarization is independent of the lepton flavor (as expected). The corresponding asymmetries have zero values near the zero recoil, while they approach -1 in the large recoil regions.
- $P_\ell^{(\Lambda_c)}(q^2)$: For the longitudinal lepton polarization of the charged lepton, it is found that for muon mode, this observable has the least variation and has almost constant value $P_\mu^{(\Lambda_c)} \simeq -1$ in the whole region. While for the tauonic mode, the behavior is quite different from the former one. $P_\tau^{(\Lambda_c)} = -0.529(13)$ at the zero recoil, and $P_\tau^{(\Lambda_c)} = 0.241(15)$ at the $q^2 = m_\tau^2$, and zero crossing occurs at $\mathbf{q_0^2 = 4.733(125) GeV^2}$.
- $C_F^\ell(q^2)$: The convexity parameter has zero value for both the decay modes at zero recoil value. At the large recoil range at $q^2 = 0.45 GeV^2$, C_F^μ reaches its maximum value $-1.297(16)$ and due to lepton mass effect it becomes zero suddenly at $q^2 = m_\mu^2$. Where as C_F^τ has a very low value throughout the q^2 region and reaches its maximum value, $-0.146(9)$ at $q^2 = 6.45 GeV^2$.
- Note that the predictions shown in tables 5 and 6, respectively, are very much consistent with each other in both the parametrization of the form factors. In q^2 -bins, we can predict the normalised decay rates and the angular observables in both the leptonic modes with an error

Obs.	Parametrization	q^2 bin (in GeV^2)				
		q_{\min}^2 -5	5-7	7-9	9- q_{\max}^2	q_{\min}^2 - q_{\max}^2
$\langle \frac{\Gamma}{ V_{cb} ^2} \rangle$	BCL	0.0059(5)	0.024(2)	0.034(2)	0.029(2)	0.092(5)
	BGL	0.0060(5)	0.024(2)	0.034(2)	0.029(2)	0.093(5)
$\langle A_{FB}^\tau \rangle$	BCL	0.272(14)	0.113(12)	-0.002(7)	-0.050(4)	tab. 7
	BGL	0.273(14)	0.115(12)	-0.001(7)	-0.050(4)	-
$\langle A_{FB}^{\Lambda_c \tau} \rangle$	BCL	0.108(13)	0.034(7)	-0.029(5)	-0.084(10)	tab. 7
	BGL	0.109(13)	0.035(7)	-0.029(5)	-0.084(10)	-
$\langle A_{FB}^{\Lambda_c} \rangle$	BCL	0.403(43)	0.382(41)	0.339(37)	0.218(24)	0.344(37)
	BGL	0.403(43)	0.383(41)	0.339(37)	0.218(24)	0.345(37)
$\langle P_{\Lambda_c} \rangle$	BCL	-0.958(9)	-0.908(11)	-0.804(13)	-0.509(12)	-0.761(12)
	BGL	-0.958(9)	-0.908(11)	-0.804(13)	-0.509(12)	-0.761(12)
$\langle P_\tau^{\Lambda_c} \rangle$	BCL	0.088(17)	-0.156(16)	-0.336(13)	-0.472(12)	-0.258(16)
	BGL	0.095(17)	-0.150(16)	-0.333(13)	-0.471(12)	-0.254(16)
$\langle C_F^\ell(q^2) \rangle$	BCL	-0.069(4)	-0.141(9)	-0.125(9)	-0.053(4)	-0.096(6)
	BGL	-0.069(3)	-0.140(9)	-0.125(8)	-0.053(4)	-0.096(6)

Table 6: Bin-wise observables prediction for $\Lambda_b \rightarrow \Lambda_c (\rightarrow \Lambda \pi) \tau \bar{\nu}_\tau$ mode

$\lesssim 10\%$ at $1\text{-}\sigma$. Also, for most of the observables, the predictions obtained after an integration in the full q^2 regions have an error $\approx 10\%$ at their $1\text{-}\sigma$ C.I.

- Among the angular observables, we could predict, for both the lepton final states, the Λ_c polarization asymmetry with a $1\text{-}\sigma$ error $\lesssim 2\%$.
- We obtain the muon polarization asymmetry $P_\mu^{\Lambda_c}(q^2)$ with a $1\text{-}\sigma$ error of 0.1% while the τ polarization asymmetry has an error 6% at $1\text{-}\sigma$.
- The q^2 distributions of $A_{FB}^\mu(q^2)$ and $A_{FB}^{\Lambda_c \mu}(q^2)$ in fig. 2 show that for $q^2 \rightarrow m_\mu^2$ the corresponding values suddenly increases. This region of q^2 is close to the zero crossing of $A_{FB}^\mu(q^2)$ and $A_{FB}^{\Lambda_c \mu}(q^2)$, respectively. Hence for these observables, instead of integrating over the full q^2 regions, we have predicted them for $q^2 > q_0^2$ and $q^2 < q_0^2$ which are shown in table 7. In the same table, we have also given the predictions $A_{FB}^\tau(q^2)$ and $A_{FB}^{\Lambda_c \tau}(q^2)$ for $q^2 > q_0^2$ and $q^2 < q_0^2$ where q_0^2 are the corresponding values of q^2 at the zero crossings.

Modes	q^2 Range	$\langle A_{FB}^\ell \rangle$	$\langle A_{FB}^{\Lambda_c \ell} \rangle$
τ	$[q_{\min}^2 - q_0^2]$	0.174(13)	0.075(10)
	$[q_0^2 - q_{\max}^2]$	-0.041(4)	-0.057(7)
μ	$[q_{\min}^2 - q_0^2]$	0.246(2)	0.104(11)
	$[q_0^2 - q_{\max}^2]$	-0.170(11)	-0.106(13)

Table 7: We provide predictions for the asymmetric observables, $\langle A_{FB}^\ell \rangle$ and $\langle A_{FB}^{\Lambda_c \ell} \rangle$, on both sides of their respective zero crossing values (q_0) in τ and μ modes. Refer to the text for the observables' zero crossing value (q_0).

As mentioned earlier, there are a couple of other angular observables, like K_{3s} , K_{3sc} , K_{2ss} , K_{2cc} , K_{2c} , K_{1ss} , K_{1cc} , K_{1c} , which could be extracted from the given angular distribution in eq. 2.42. The SM predictions of all these observables are given in the appendix (table 14).

Apart from the predictions of decay rates and angular observables, we have predicted the ratio of the decay rates

$$R(\Lambda_c) = \frac{\mathcal{B}(\Lambda_b \rightarrow \Lambda_c \tau \bar{\nu}_\tau)}{\mathcal{B}(\Lambda_b \rightarrow \Lambda_c \mu \bar{\nu}_\mu)}. \quad (4.2)$$

In the SM, with the BGL parametrization of the form factors, our prediction is given by

$$R(\Lambda_c) = 0.330 \pm 0.010. \quad (4.3)$$

which is consistent with the respective value obtained in [40] where BCL parametrization had been used. Therefore, the unitarity relations described earlier for the BGL coefficients have negligible impact on all the predictions. We also estimate q^2 integrated branching fraction for $\Lambda_b \rightarrow \Lambda_c^+ (\rightarrow \Lambda \pi^+) \ell \bar{\nu}_\ell$:

$$\frac{1}{|V_{cb}|^2} \times \mathcal{B}(\Lambda_b \rightarrow \Lambda_c (\rightarrow \Lambda \pi) \tau \bar{\nu}_\tau)_{\text{SM}} = 0.136(8), \quad \frac{1}{|V_{cb}|^2} \times \mathcal{B}(\Lambda_b \rightarrow \Lambda_c (\rightarrow \Lambda \pi) \mu \bar{\nu}_\mu)_{\text{SM}} = 0.413(30) \quad (4.4)$$

with, $|V_{cb}| = 40.3(5) \times 10^{-3}$ as in ref [10] and $\tau_{\Lambda_b}^{\text{HFLAV}} = 1.471(9)$ ps [58].

$$\mathcal{B}(\Lambda_b \rightarrow \Lambda_c (\rightarrow \Lambda \pi) \tau \bar{\nu}_\tau)_{\text{SM}} = 2.21(14) \times 10^{-4} \quad \text{and,} \quad \mathcal{B}(\Lambda_b \rightarrow \Lambda_c (\rightarrow \Lambda \pi) \mu \bar{\nu}_\mu)_{\text{SM}} = 6.70(52) \times 10^{-4}. \quad (4.5)$$

5 Test of New Physics with existing observations: One and two Operator scenario

A few other lepton flavor violating ratios, like $R(D^{(*)}) = \Gamma(B \rightarrow D^{(*)} \tau^- \bar{\nu}) / \Gamma(B \rightarrow D^{(*)} \ell^- \bar{\nu})$ and $R(J/\psi) = \Gamma(B_c \rightarrow J/\psi \tau^- \bar{\nu}) / \Gamma(B_c \rightarrow J/\psi \ell^- \bar{\nu})$ are measured by the experimental collaborations BaBar, Belle, and LHCb, respectively [28–38]. A global average of these quantities is available HFLAV [1],

$$R(D) = 0.357 \pm 0.029, \quad (5.1)$$

$$R(D^*) = 0.284 \pm 0.012. \quad (5.2)$$

Based on the most recent lattice inputs, the corresponding SM predictions are given by [10]

$$R(D)_{\text{SM}} = 0.304 \pm 0.003, \quad (5.3)$$

$$R(D^*)_{\text{SM}} = 0.258 \pm 0.012. \quad (5.4)$$

At the moment, the measurements have relatively large errors, and the SM prediction of $R(D^*)$ has a relatively large error as compared to $R(D)$. In the present scenario, the data deviates from the respective SM predictions at $\approx 2\sigma$. Note that the measurements on $R(D)$ and $R(D^*)$ also have some correlation due to which there will be little more discrepancies than 2σ [1].

Recently, LHCb has measured $\mathcal{B}(\Lambda_b \rightarrow \Lambda_c \tau \bar{\nu})$ and finds [52],

$$R(\Lambda_c) = 0.242 \pm 0.026 \pm 0.040 \pm 0.059 \quad (5.5)$$

where the first uncertainty is statistical, the second is systematic and the third is due to external branching fraction measurements. In comparison to our SM prediction,

$$R(\Lambda_c)_{\text{SM}} = 0.330 \pm 0.010, \quad (5.6)$$

it points towards a downward shift. The data is consistent with the SM prediction within 1.15σ uncertainties.

Note that in the measurement for $R(\Lambda_c)$, to normalize $\Lambda_b \rightarrow \Lambda_c \tau \nu$ decay rate, LHCb have used $\mathcal{B}(\Lambda_b \rightarrow \Lambda_c \mu \nu)_{\text{DELPHI}} = 6.2(1.4)\%$ which is measured by DELPHI collaboration [59]. Using this data we have obtained an estimate for $|V_{cb}|$ which is as given below

$$|V_{cb}| = (37.9 \pm 4.5) \times 10^{-3}. \quad (5.7)$$

This estimate has large error but consistent with those obtained from $B \rightarrow D^{(*)}(\mu, e)\nu$ modes [10]. At the same time we have utilised the measured value $\mathcal{B}(\Lambda_b \rightarrow \Lambda_c \tau \nu) = (1.5 \pm 0.16 \pm 0.25 \pm 0.23)\%$ [52] and have obtained

$$|V_{cb}| = (44.0 \pm 5.0) \times 10^{-3}. \quad (5.8)$$

Both of these estimates are consistent within their 0.91σ uncertainties, though they have large errors and there is a gap of about 16% between the two best fit values. In the context of NP effects in these modes, it is important to note that $\Lambda_b \rightarrow \Lambda_c \tau \nu$ could be potentially sensitive to contributions beyond the SM.

Many model independent NP analysis have been performed to explain either the deviation observed in $R(D)$ and $R(D^*)$ [10, 13, 16, 18, 22, 24, 26] and with $R(\Lambda_c)$ [39, 44–48, 50] alone with NP effects that appears through only tauonic interaction to the theory. However, a simultaneous explanation of these three LFUV ratios is mandatory, because the three decay modes are correlated through the same charge current interaction. Therefore to critically scrutinize the compatibility of data under the presence of NP scenarios we do a combined χ^2 fit to these observables. However, an analogous behavior has been observed for $R(J/\psi)$, the measured values are by LHCb [60]

$$R(J/\psi)|_{\text{LHCb}} = 0.71 \pm 0.17 \pm 0.18, \quad (5.9)$$

and by CMS [61]

$$R(J/\psi)|_{\text{CMS}} = 0.17 \pm 0.33. \quad (5.10)$$

Note that both the measurements have large errors, and they agree with each others at their 1.3σ error. The corresponding SM prediction to compare is given by [62] (HPQCD lattice collaboration)

$$R(J/\psi) = 0.258 \pm 0.004. \quad (5.11)$$

The SM prediction is compatible with LHCb at the 1.8σ level, while measured value by CMS is consistent with the SM predictions within their 1σ error. We would like to wait for a little more precise data to incorporate these inputs in the analysis of NP. Another essential point is that for this mode, the inputs on the vector form factors are available, but the inputs on the tensor form factors are not available. Later, we will see that the contributions from the tensor current operator will play an essential role to explain the other available data. In the following subsections, we will discuss the results of the analyses of the extractions of new physics from different fits to the available data.

5.1 New Physics analysis: One operator scenario

The new physics effective operators relevant to $b \rightarrow c \tau^- \bar{\nu}$ transitions are defined in eqn.2.1. The relevant data on $B \rightarrow D^{(*)} \mu^- \bar{\nu}$ decays suggest that the allowed new physics contributions in $b \rightarrow c \mu^- \bar{\nu}$ transitions are negligibly small [10], which is as per the expectations. To constrain the new WCs, we first do the fit to the available data considering the contributions from one operator at a time. We perform a combine analysis of $R(D)$, $R(D^*)$, $R(\Lambda_c)$, $F_L^{D^*}$ and $\mathcal{B}(\Lambda_b \rightarrow \Lambda_c \tau \nu)$ observables. We have used global average data (central value and uncertainty) for $R(D)$

and $R(D^*)$ observables along with their correlation, which were computed by the Heavy Flavor Averaging Group (HFLAV) [1], as input in our analysis. Furthermore, we included the latest LHCb measurement, which is the only single measurement, for the data on $\mathcal{B}(\Lambda_b \rightarrow \Lambda_c \tau \nu)$ and $R(\Lambda_c)$ [52]. In addition, we have incorporated the recent measurement on $F_L^{D^*}$ by LHCb [53]. In table 8, we have presented the data used in the fit along with the corresponding references. We closely

$\mathbf{R}(D)$ [1]	$\mathbf{R}(D^*)$ [1]	correlation [1]	$\mathbf{R}(\Lambda_c)$ [52]	$\mathcal{B}(\Lambda_b \rightarrow \Lambda_c \tau \bar{\nu}_\tau)$ [52]	$\mathbf{F}_L^{D^*}$ [53]
0.357(29)	0.284(12)	-0.37	0.242(76)	0.015(4)	0.43(7)

Table 8: Experimental data used in the fit.

follow the treatment in ref [10] for the observables $R(D)$, $R(D^*)$ and $F_L^{D^*}$. For our purposes, we have taken the analytic expressions for the observables $R(D)$ and $R(D^*)$ as well as $F_L^{D^*}$ from that reference. We provide the relevant expressions in the Appendix [8.6]. The new WCs are the only free parameters in these expressions. We also quote the error in SM predictions, which are shown as the overall normalization in the respective expressions. In the analysis in [10], the shape of the form factors is obtained using only the lattice inputs, and the estimated errors in SM are solely due to the form factors. In the NP scenarios, the additional error will come from the uncertainties in the fitted values of the new WCs. The shape of the $B \rightarrow D$ transition form factors are obtained using the lattice inputs from Fermilab-MILC collaboration [63] and the HPQCD collaboration [64]. For the $B \rightarrow D^*$ decay, the inputs on the form factors are taken from the Fermilab-MILC and JLQCD collaboration [65, 66]. For $\Lambda_b \rightarrow \Lambda_c \tau^- \bar{\nu}$ decay we have obtained the shape of all the form factors relevant in NP scenarios from lattice [40, 43]. In addition to $R(D)$, $R(D^*)$, $R(\Lambda_c)$ and longitudinal polarization $F_L^{D^*}$, we have used the total branching fraction $\mathcal{B}(\Lambda_b \rightarrow \Lambda_c \tau \bar{\nu}_\tau)$ as input in our analysis.

To perform a model-independent analysis, we did the χ^2 -fit to the data given in table 8 with different NP hypothesis. The χ^2 function is defined as

$$\chi^2(C_k) = \sum_{i,j} [\mathcal{O}_i^{th}(C_k) - \mathcal{O}_i^{exp}] (V^{exp} + V^{th})_{i,j}^{-1} [\mathcal{O}_i^{th}(C_k) - \mathcal{O}_i^{exp}]. \quad (5.12)$$

We have minimized this χ^2 function. Here, \mathcal{O}_i^{exp} and \mathcal{O}_i^{th} are the respective measured values and the theoretical expressions of the observables, and C_k 's are the Wilson coefficients of the effective Hamiltonian in eq. 2.1. $V_{i,j}^{exp(th)}$ is the corresponding measured (theoretical) covariance matrix. Therefore, observable uncertainties and their correlation can be taken care of through the covariance matrix. Here, the theory correlations will be between $R(D^*)$ and $F_L^{D^*}$, and between $R(\Lambda_c)$ and $\mathcal{B}(\Lambda_b \rightarrow \Lambda_c \tau \nu)$.

The fit results for each NP scenario taken one at a time, are listed in table 9. We also use p-value to determine how likely a hypothesis is to be true based on the measured data. It is a quantitative measure of compatibility between the hypothesis and measurement. It is calculated using the following formula :

$$\text{p-value} = 1 - \text{CDF}_{d.o.f}(\chi_{min.}^2) \quad (5.13)$$

The CDF_n is the cumulative distribution function of a random variable that follows the χ^2 -distribution with degrees of freedom n at the value of the variable χ_{min}^2 (the value of χ_{min}^2 is the best-fit point value of $\chi^2(C_k)$). The p-value for each of the fit scenarios is presented in the table 9. Note that in all the cases we have allowed fit, however, the scenario with \mathcal{O}_{V_2} have relatively low p-value. To identify the reason for this observation, we predict the values of these observables in

Parameter	One Parameter fit scenario			σ_{dev} (in σ)		
	Fit values	$\chi^2_{min.}/DOF$	P-Value	$R(D)$	$R(D^*)$	$R(\Lambda_c)$
$Re[C_{S_1}]$	0.104(45)	4.463/4	0.215	0.151	1.355	1.372
$Re[C_{S_2}]$	0.101(47)	5.187/4	0.159	0.098	1.709	1.297
$Re[C_{V_1}]$	0.050(22)	4.001/4	0.261	0.683	0.048	1.524
$Re[C_{V_2}]$	-0.0045(339)	9.176/4	0.027	1.564	1.029	1.128
$Re[C_T]$	-0.022(18)	7.903/4	0.048	1.971	0.343	1.385

Table 9: The simultaneous fit of the new physics WCs(one parameter scenario) and form-factors parameter. The inputs are $R(D)$, $R(D^*)$, $R(\Lambda_c)$, $F_L^{D^*}$, $\mathcal{B}(\Lambda_b \rightarrow \Lambda_c \tau \nu)$. These fit consider NP only in τ final state. Also, we quantify the tension between observable and corresponding observational data for each scenario and present it in the last three columns.

Observables	Observables Prediction(One operator scenario)					Expt. Measurement
	$Re[C_{S_1}]$	$Re[C_{S_2}]$	$Re[C_{V_1}]$	$Re[C_{V_2}]$	$Re[C_T]$	
$\mathbf{R}(D)$	0.363(27)	0.361(29)	0.335(14)	0.301(21)	0.299(5)	0.357(29) [1]
$\mathbf{R}(D^*)$	0.261(12)	0.255(12)	0.285(17)	0.260(20)	0.276(20)	0.284(12) [1]
$\mathbf{R}(\Lambda_c)$	0.348(14)	0.342(13)	0.361(18)	0.329(13)	0.352(23)	0.242(76)[52]
$\mathbf{F}^{\ell}(D^*)$	0.433(3)	0.421(3)	0.427(9)	0.427(3)	0.421(6)	0.430(70) [53]
$\mathbf{P}^{\tau}(D^*)$	-0.502(10)	-0.535(9)	-0.519(7)	-0.519(7)	-0.505(14)	-0.38(54) [34]
$\mathbf{P}^{\tau}(D)$	0.433(42)	0.431(45)	0.324(3)	0.324(3)	0.336(10)	N.A.

Table 10: Predictions of $R(D)$, $R(D^*)$, $R(\Lambda_c)$ and $F_L^{D^*}$ using the corresponding fit results from tab [9] considering new physics only in τ channel. The deviation between the theory prediction and the experimental observation is also presented in the unit of σ .

all these NP scenarios which we have presented in table 10. We have further estimated the tension between the data and our NP predictions by defining the following quantity

$$\sigma_{dev} = \left| \frac{\mathcal{O}_i^{exp} - \mathcal{O}_i^{NP}}{\sqrt{\sigma_i^2|_{exp} + \sigma_i^2|_{NP}}} \right|. \quad (5.14)$$

It is a quantitative measure of the deviation between observed data and the prediction of the observables in the presence of the NP fit scenario (see tab. 9). One can infer from these estimates that none of the one-operator scenarios could explain all three data simultaneously. The situation is even worse in the case of \mathcal{O}_{V_2} , none of the three data could be explained within their 1σ confidence interval (CI). In table 10, along with $R(D)$, $R(D^*)$, $R(\Lambda_c)$ and $F_L^{D^*}$ we have also estimated the τ polarisation asymmetries $P^{\tau}(D^*)$ and $P^{\tau}(D)$. Measurement is also available on $P^{\tau}(D^*)$ which we have shown in the same table. We have not included it in our analysis since the error in the measurement is too large. Also, in all the NP scenarios the predictions are negative and consistent with the measured value. Note that the deviations shown in table 9 represent the deviations of each of the observables with the respective data. However, as we know all the observables will be correlated due to similar type new physics effects. We have worked out these correlations in different one operator scenarios which are shown in fig. 3. Also, we have shown the correlations between the $P^{\tau}(D^*)$ and $R(\Lambda_c)$ in each of the one operator scenarios. In the following items we will decode the informations in these plots.

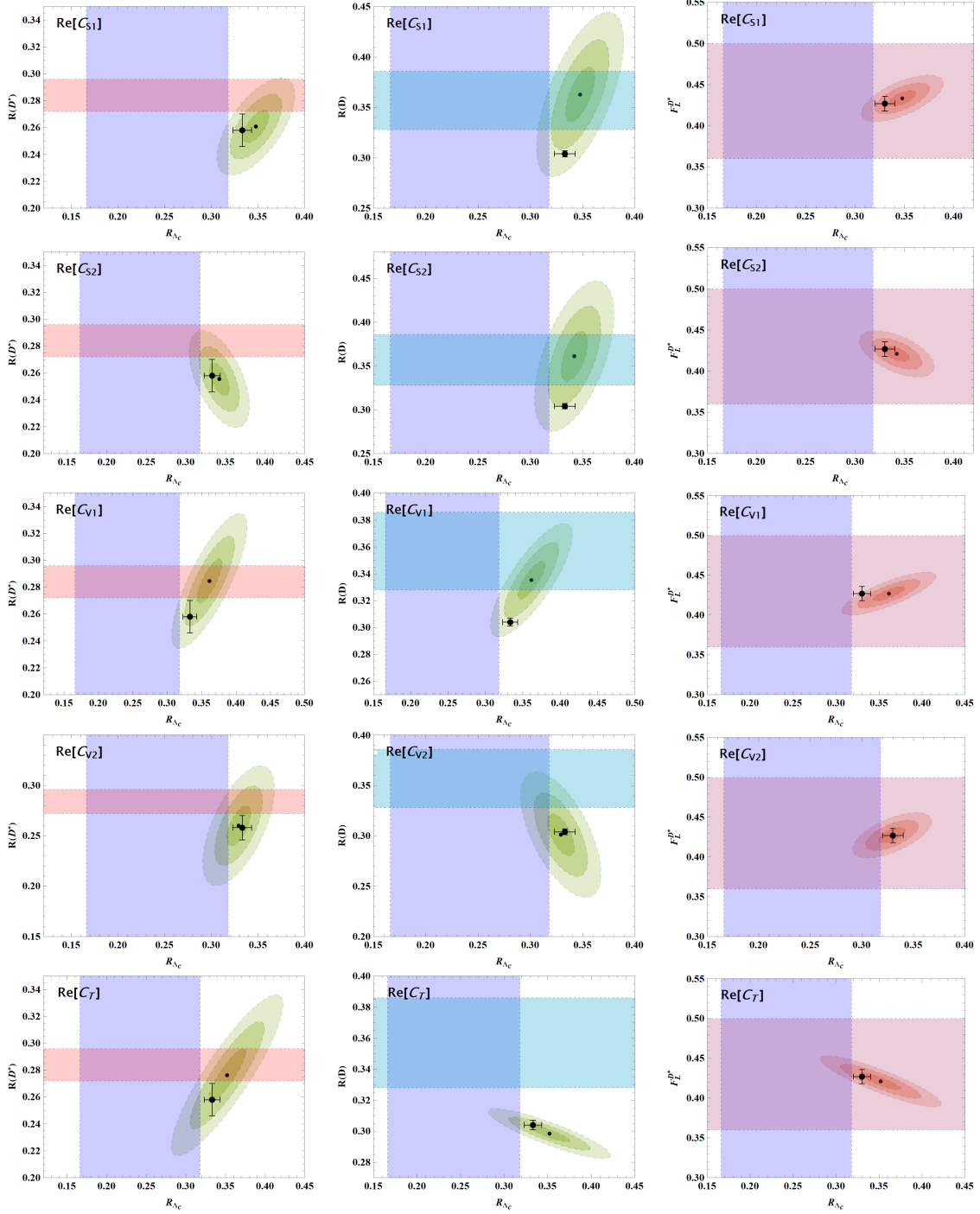


Figure 3: The correlation of $R(D)$, $R(D^*)$, $F_L^{D^*}$ with $R(\Lambda_c)$ in different one-parameter scenarios. The horizontal and vertical color bands represent the respective experimental results at their 1σ CI. The correlations between the observables are represented by ellipses. We have shown the 1σ , 2σ , and 3σ contour error bands around the best estimate point (black) using the best-fit point (given in table [9]). The SM estimation has also been shown using a black point with vertical and horizontal 1σ error bars for the respective observables.

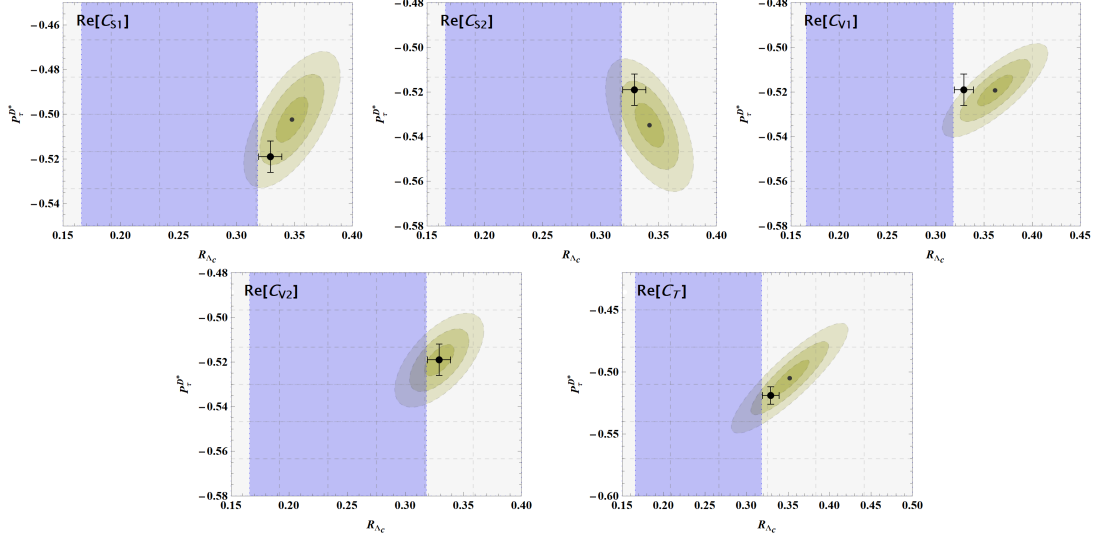


Figure 4: Correlation plots between $P_\tau^{D^*}$ and $R(\Lambda_c)$ in one operator scenario. Vertical color bands represent the experimental constraints measure for $R(\Lambda_c)$ within 1σ confidence level whereas full parameter space is allowed for $P_\tau^{D^*}$ for each of the NP scenario. The correlations between the observables are represented by ellipses. We have shown the 1σ , 2σ , and 3σ contour error bands around the best estimate point (black) using the best-fit point (given in table [9]). The SM estimation has also been shown using a black point with vertical and horizontal 1σ error bars for the respective observables.

- In all the scenarios, we can explain the data on $F_L^{D^*}$ and $P^\tau(D^*)$, the 1σ contours are well within the current experimental limits.
- Suppose we take the errors of our predictions within 3σ . In that case, we can comfortably explain the data on $R(D)$ and $R(D^*)$ simultaneously in all the scenarios except the scenario with \mathcal{O}_T . Among these, the scenario with \mathcal{O}_{V_1} is the most preferred, in which both the data could be explained within their respective 1σ bands.
- In all the scenarios, independently, we could explain a small portion (relatively higher values) of the current experimental limit on $R(\Lambda_c)$ if we consider the respective 3σ contours. We can do it more comfortably with \mathcal{O}_T and with \mathcal{O}_{V_2} .
- The predictions of table 10 and the correlation plots in fig. 3 and 4 suggest that if we consider the errors within their 1σ CI, none of the one operator scenarios can explain the current data on $R(D)$, $R(D^*)$, $F_L^{D^*}$, $P^\tau(D^*)$ and $R(\Lambda_c)$ simultaneously. However, if we consider the 3σ contours of our predictions, then only the scenarios with the operator \mathcal{O}_{S_2} or \mathcal{O}_{V_2} could explain these five data simultaneously. Again, we can explain only a tiny portion of the current experimental limit on $R(\Lambda_c)$.

The correlation plots are also helpful in understanding how the conclusions may change based on the modifications in more precise data in the near future. For example, if the future data shows only deviations in $R(D)$ but not in $R(D^*)$, then this will indicate scalar-pseudoscalar type interactions. On the other hand, if we see the deviations in both these measurements, a new $(V \pm A)$ type of interaction will provide the more probable solutions. Of course, more precise measurements of the other observables will further shed light on a particular type of new interaction in case of deviations, which is also clear from these correlation plots. We have also estimated the values of all the other

Observables	Re[C_{S_1}]	Re[C_{S_2}]	Re[C_{V_1}]	Re[C_{V_2}]	Re[C_T]	SM
\hat{K}_{1cc}	0.3131(13)	0.3127(13)	0.3120(13)	0.3120(14)	0.3131(15)	0.3120(25)
\hat{K}_{1ss}	0.34343(66)	0.34363(65)	0.34402(65)	0.34398(70)	0.34346(75)	0.34399(65)
\hat{K}_{2cc}	0.208(22)	0.203(22)	0.208(22)	0.207(23)	0.194(25)	0.208(22)
\hat{K}_{2ss}	0.239(26)	0.235(26)	0.241(26)	0.240(26)	0.224(28)	0.240(26)
\hat{K}_{3sc}	0.0162(22)	0.0165(22)	0.0172(23)	0.0171(23)	0.0160(23)	0.0172(23)
\hat{K}_{3s}	0.0337(84)	0.0324(89)	0.0432(81)	0.045(13)	0.0471(87)	0.0436(81)
A_{FB}^{ℓ}	0.118(12)	0.108(11)	0.104(11)	0.104(11)	0.108(11)	0.103(11)
$A_{FB}^{\Lambda_c \ell}$	0.0280(74)	0.0242(67)	0.0190(62)	0.0182(78)	0.0141(74)	0.0184(62)
$A_{FB}^{\Lambda_c}$	0.343(37)	0.336(37)	0.345(37)	0.344(38)	0.321(41)	0.344(37)
P_{Λ_c}	-0.758(12)	-0.741(16)	-0.763(12)	-0.760(21)	-0.705(51)	-0.761(12)
$P_{\tau}^{(\Lambda_c)}$	-0.187(35)	-0.207(30)	-0.257(16)	-0.260(26)	-0.260(15)	-0.258(16)
C_F^{ℓ}	-0.091(6)	-0.093(6)	-0.096(6)	-0.096(6)	-0.091(7)	-0.096(6)

Table 11: Predictions for the angular observables with the fit results given in table [9], considering NP one at a time.

angular observables related to $\Lambda_b \rightarrow \Lambda_c^+(\rightarrow \Lambda\pi)\tau^-\bar{\nu}_\tau$ in all these one operator scenarios in table 11 which can be compared with the respective SM predictions and with the future measurements. These results are obtained using the fit values given in table 9. Given the errors in the predictions, at the moment, it would be hard to distinguish the NP effects in those observables from the respective SM predictions. We need more precise results from lattice to improve the predictions.

From eqn. 2.42, we see that unpolarised initial baryon decay gives ten observables with different helicity combinations. We expect that with the next runs, LHCb can measure these observables. In this work, we have analysed the NP sensitivities of these observables throughout the allowed q^2 regions. The results are presented in fig. 5. Considering the allowed values of the new WCs obtained in table 9, we restrict the values of the new WCs to generate these plots. We have presented the corresponding results in fig. 5 for $Re(C_i) = 0.1$ (solid lines) and $Re(C_i) = -0.1$ (dashed line), respectively. Note that once we are able to reduce the errors in our estimates, the one operator scenario with \mathcal{O}_T might show deviations in a couple of those observables, which could be distinguished from the respective SM predictions. However, suppose data in the future allows $|Re(C_i)| \approx 1$. In that case, the situation may change, and in a few more new physics scenarios, we may see deviations in these observables, which is beyond the scope of this paper.

All these observation pointed out so far motivates us to look for impact of two operator scenarios in all these observables. In the following subsection we will present the results of the two operator analysis.

5.2 New physics analysis: Two operators scenario

Following the discussion in the last subsection, we have separately studied the impact of the two-operator scenarios. Also, while analyzing the contributions to the decay rate due to scalar, pseudo-scalar, and tensor type operators, we notice terms which are due to the interference between different operators (like $C_i C_j$), and those terms are dependent on m_ℓ . So for $m_\ell = m_\mu$ these terms will be small can be ignored, but for $m_\ell = m_\tau$, while considering the NP present one at a time to our theory, these massive contributions remain left out. Hence, the study of the two operator scenarios will be important to incorporate and understand the impact of these mass-dependent interference terms, which will be otherwise missing in the one operator scenarios. Also, for simplicity we have considered only the real WCs.

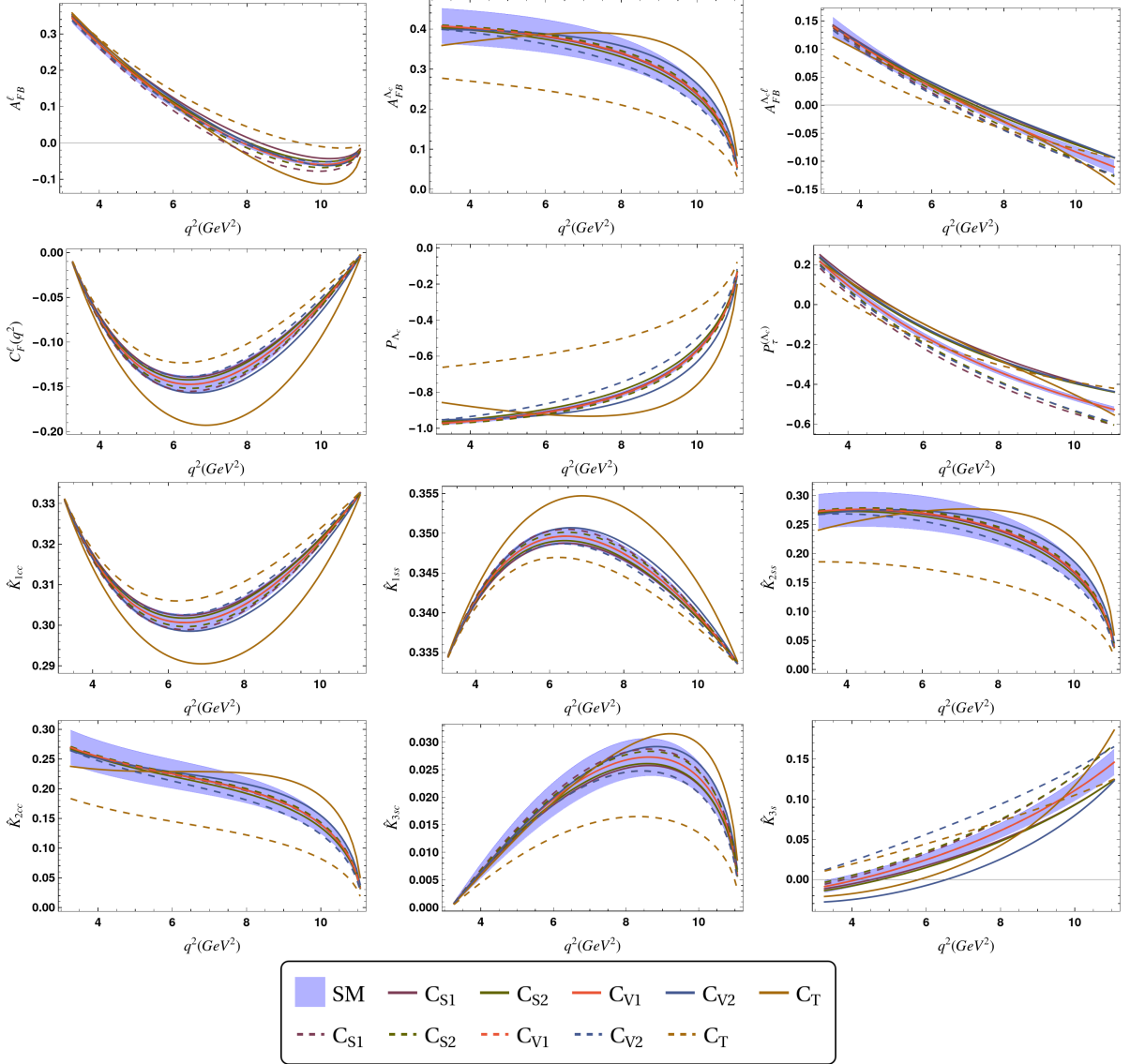


Figure 5: The q^2 dependence of the angular observables for $\Lambda_b \rightarrow \Lambda_c(\rightarrow \Lambda\pi)\tau\bar{\nu}_\tau$ decay in the one operator scenarios with $C_i = 0.1$ (solid line) and $C_i = -0.1$ (dashed line).

We provide a detailed discussion for each of the angular distributions in the presence of one and two NP operators along with SM. In our analysis, we normalize each observable with the decay rate, which is $2K_{1ss} + K_{1cc}$. This makes the observables independent of $|V_{cb}|$. The observables are then dependent only on the hadronic helicity amplitude, which is parameterized by form factors. In the subsequent section, we use the BCL parameterization for form factor shape. To check the NP sensitivities of these observables, using the form factors as an external input, we obtain the q^2 shapes of the observables under consideration. The table 12 presents our fit results for each two-parameter scenario. Using these fit results, we obtain the predictions of all the related observables in tables 14 and 15, respectively, in the appendix. Among these we compare the predictions of $R(D)$, $R(D^*)$, $F_L^{D^*}$ and $R(\Lambda_c)$ with the respective measured values and estimated the deviations (σ_{dev}) using the formula given in eqn. 5.14. Note that if we consider the 1σ error in the respective predictions, in all the two operator scenarios we can explain the measured observables in $B \rightarrow D^{(*)}\tau^-\bar{\nu}$ decays. However, the scenario with $[\mathcal{O}_{S_2}, \mathcal{O}_T]$ is the only two-operator scenario which could accommodate

2 Operator Scenario	Two operator scenarios fit results				σ_{dev} (in σ)			
	WC fit results		χ^2_{min}/DOF	P-Value	R(D)	R(D*)	R(Λ_c)	$F_L^{D^*}$
C_{S_1}, C_{S_2}	Re[C_{S_1}]	-2.268(207)	3.432/3	0.330	0.067	0.409	1.437	0.237
	Re[C_{S_2}]	0.904(220)						
C_{S_1}, C_T	Re[C_{S_1}]	0.098(46)	3.978/3	0.264	0.038	0.526	1.494	0.010
	Re[C_T]	-0.014(19)						
C_{S_2}, C_T	Re[C_{S_2}]	-1.255(64)	1.553/3	0.670	0.039	0.391	0.963	0.278
	Re[C_T]	0.226(32)						
C_{V_1}, C_{V_2}	Re[C_{V_1}]	-0.978(32)	3.557/3	0.313	0.113	0.303	1.503	0.013
	Re[C_{V_2}]	1.055(23)						
C_{V_1}, C_T	Re[C_{V_1}]	0.077(31)	2.827/3	0.419	0.148	0.466	1.296	0.006
	Re[C_T]	0.037(37)						
C_{V_2}, C_T	Re[C_{V_2}]	0.080(53)	5.829/3	0.120	0.435	0.560	1.634	0.389
	Re[C_T]	-0.059(28)						
C_{S_1}, C_{V_1}	Re[C_{S_1}]	0.051(73)	3.534/3	0.316	0.102	0.311	1.498	0.0004
	Re[C_{V_1}]	0.033(34)						
C_{S_1}, C_{V_2}	Re[C_{S_1}]	0.123(48)	3.511/3	0.319	0.106	0.301	1.494	0.098
	Re[C_{V_2}]	-0.033(33)						
C_{S_2}, C_{V_1}	Re[C_{S_2}]	0.045(65)	3.533/3	0.316	0.101	0.311	1.496	0.079
	Re[C_{V_1}]	0.038(29)						
C_{S_2}, C_{V_2}	Re[C_{S_2}]	0.139(54)	3.474/3	0.324	0.104	0.292	1.489	0.098
	Re[C_{V_2}]	-0.048(36)						

Table 12: Fit results for the simultaneous fit of the NP Wilson coefficients (in the two-operator scenario) and form-factor parameters. The inputs used in the fit are $R(D)$, $R(D^*)$, $R(\Lambda_c)$, $F_L^{D^*}$ and $\mathcal{B}(\Lambda_b \rightarrow \Lambda_c \tau \bar{\nu}_\tau)$, where we only consider new physics in the τ final state. In addition, we quantify the influence of LFUV data on the corresponding fit and present the results in the last three columns.

the data on $R(\Lambda_c)$ alongside $R(D)$, $R(D^*)$, $F_L^{D^*}$ within their 1σ uncertainties. This is also the best-fit scenario which has the largest p-value i.e., 67% among all others. The correlations between the observables in the scenario $[\mathcal{O}_{S_2}, \mathcal{O}_T]$ are shown in fig. 6 which indicates that we can comfortably explain all the four data mentioned above along with $P^\tau(D^*)$, which has a relatively large error. We have also analysed the correlation between these observables in all the other two operator scenarios and noted that it is possible to simultaneously explain the data on $R(\Lambda_c)$ with $R(D)$, $F_L^{D^*}$ and $P^\tau(D^*)$, respectively if we take the 3σ contours of our predictions. However, while it is coming to a simultaneous explanation of $R(\Lambda_c)$ and $R(D^*)$, most of the scenarios fail to do so even if we consider the 3σ contours. There are too many such plots, and we have not shown them here separately.

In table 15, we have predicted the asymmetric and angular observables in $\Lambda_b \rightarrow \Lambda_c^+ (\rightarrow \Lambda \pi) \tau^- \bar{\nu}_\tau$ decays in all the two operator scenarios. These predictions are obtained using the fit results in table 12. Also, we have estimated the σ level discrepancies between the prediction in the NP scenarios and the SM. We present the corresponding results in table 13, and the scenarios showing discrepancies of more than 2σ level are pointed in bold font. Note that in the two operator scenarios, we observe discrepancies in a couple of observable which we don't see in one operator scenarios. This is due to interference terms of the two new WCs proportional to the mass of the τ -lepton which are absent in the one operator scenarios.

Note that apart from $[\mathcal{O}_{S_1}, \mathcal{O}_{S_2}]$, $[\mathcal{O}_{S_2}, \mathcal{O}_T]$ and $[\mathcal{O}_{V_1}, \mathcal{O}_{V_2}]$ in the rest of the two operator

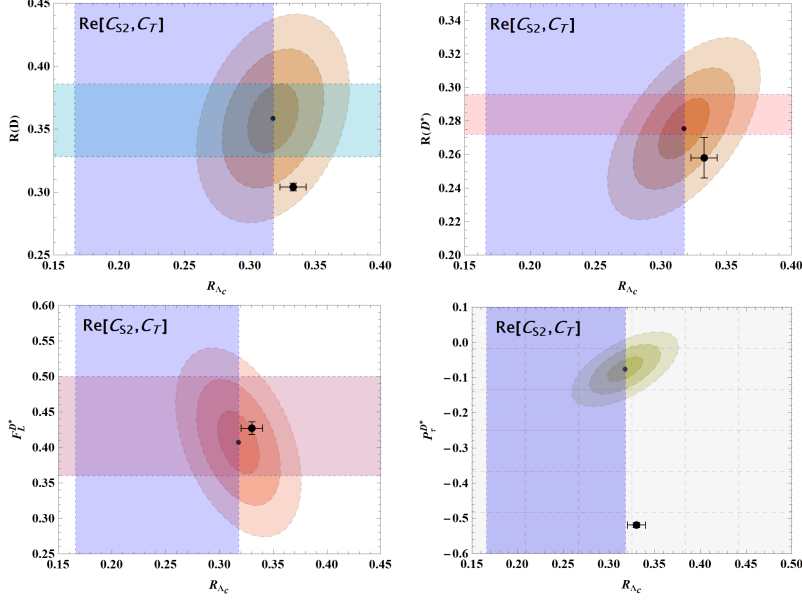


Figure 6: The plot shows the correlation between $R(D)$ and $R(\Lambda_c)$ in different NP two-parameter scenarios. The horizontal and vertical color bands represent the experimental constraints of $R(D)$ and $R(\Lambda_c)$, respectively, at a 1σ confidence level. The correlations between the observables are represented by an ellipse. We have also shown 1σ , 2σ , and 3σ contour error bands around the best estimate point (black) using the best-fit point (given in Table 12). The SM estimation has also been shown using a black point with vertical and horizontal 1σ error bars for the respective observables.

Scenario	Deviations w.r.t. SM predictions (in σ level)											
	\hat{K}_{1cc}	\hat{K}_{1ss}	\hat{K}_{2cc}	\hat{K}_{2ss}	\hat{K}_{3sc}	\hat{K}_{3s}	A_{FB}^ℓ	$A_{FB}^{\Lambda_c\tau}$	$A_{FB}^{\Lambda_c}$	P_{Λ_c}	$P_\tau^{(\Lambda_c)}$	C_F^ℓ
$[C_{S_1}, C_{S_2}]$	0.354	0.819	0.193	0.082	0.277	4.22	20.051	9.856	0.161	0.16	0.806	0.60
$[C_{S_1}, C_T]$	0.894	0.819	0.24	0.288	0.354	0.664	0.983	0.647	0.364	0.714	1.574	0.868
$[C_{S_2}, C_T]$	3.328	4.915	6.209	5.794	2.683	2.507	6.116	0.2	7.343	7.532	8.831	4.389
$[C_{V_1}, C_{V_2}]$	0.	0.	13.133	13.136	12.021	4.468	19.279	9.753	18.11	70.863	0.472	0.236
$[C_{V_1}, C_T]$	0.555	0.819	0.44	0.453	0.277	0.547	0.123	0.651	0.602	1.317	0.451	0.745
$[C_{V_2}, C_T]$	0.447	0.819	0.901	0.899	0.832	0.868	1.057	0.108	1.185	1.805	1.143	0.589
$[C_{S_1}, C_{V_1}]$	0.354	0.	0.	0.	0.	0.39	0.43	0.462	0.	0.	0.636	0.217
$[C_{S_1}, C_{V_2}]$	0.894	0.819	0.096	0.136	0.354	0.208	0.921	0.7	0.188	0.786	1.611	0.868
$[C_{S_2}, C_{V_1}]$	0.	0.	0.064	0.054	0.	0.469	0.193	0.325	0.081	0.324	0.572	0.118
$[C_{S_2}, C_{V_2}]$	0.894	0.819	0.354	0.36	0.354	0.139	0.064	0.217	0.497	1.658	1.089	0.759

Table 13: The discrepancies/agreement between the predictions in the two-operator scenarios and in the SM. The respective predictions are shown in table 15, which are obtained using the fit results of table 12.

scenarios we do not observe any significant deviations in these observables with respect to the SM. Note that in the scenario $[\mathcal{O}_{S_2}, \mathcal{O}_T]$, apart from $A_{FB}^{\Lambda_c\tau}$ almost all the other observables will show discrepancies for the corresponding SM predictions. As we can see from table 15, in this scenario, the predicted values of a couple of observables will be lower than the respective SM predictions, while in a few, they are larger than the SM. In the scenario $[\mathcal{O}_{S_1}, \mathcal{O}_{S_2}]$ we will observe deviations only in \hat{K}_{3s} , A_{FB}^τ and $A_{FB}^{\Lambda_c\tau}$ which is significant in A_{FB}^τ . The predictions of A_{FB}^τ and $A_{FB}^{\Lambda_c\tau}$ are lower

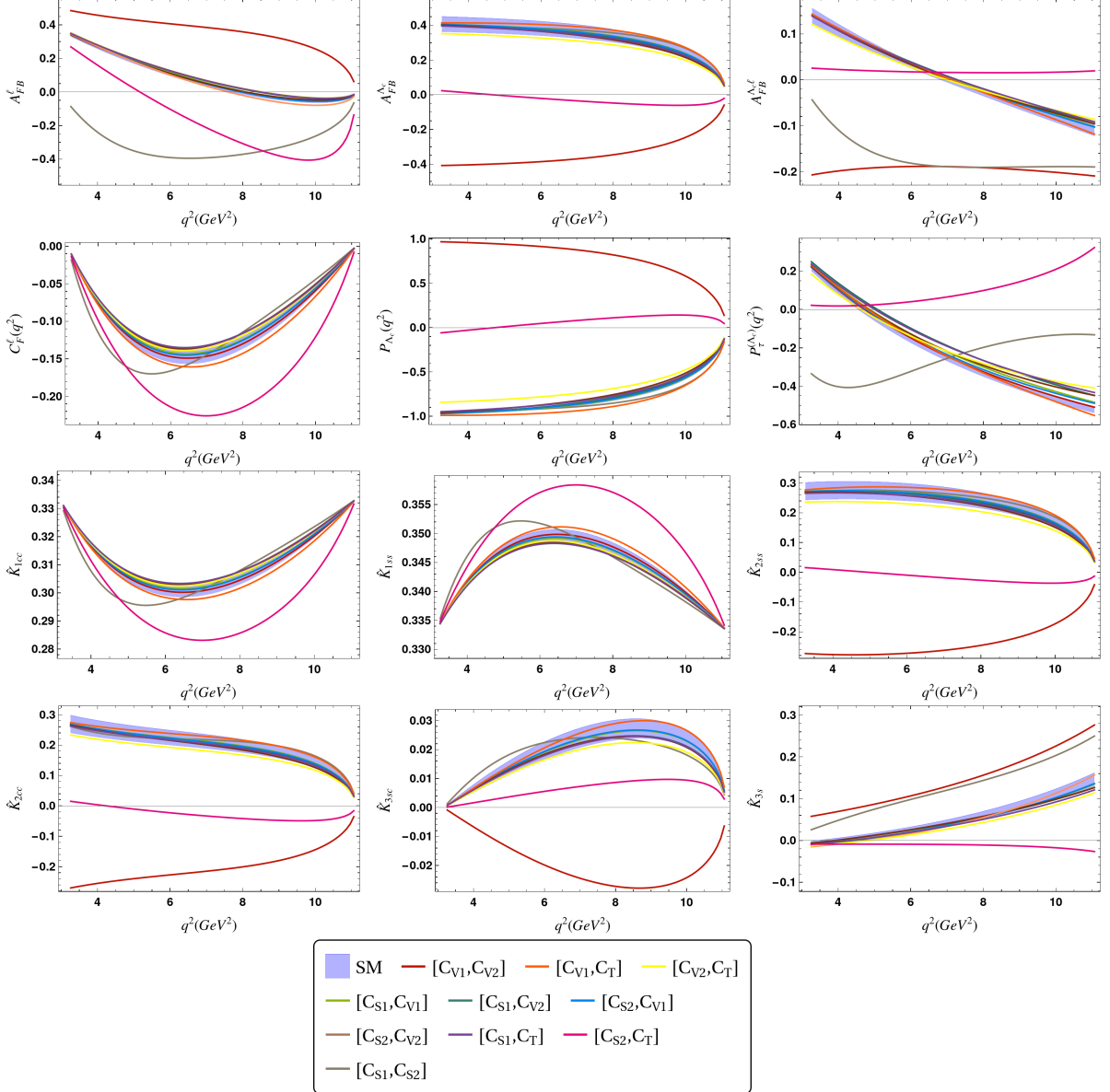


Figure 7: The q^2 dependence of the angular observables for $\Lambda_b \rightarrow \Lambda_c(\rightarrow \Lambda\pi)\tau\bar{\nu}_\tau$ decay. The variations have been shown for different NP two parameter scenarios.

than the SM and have opposite signs, while the prediction of \hat{K}_{3s} is larger than the SM. In the scenario $[\mathcal{O}_{V_1}, \mathcal{O}_{V_2}]$, apart from \hat{K}_{1cc} , \hat{K}_{1ss} and $P_\tau^{\Lambda_c}$ in the predictions of the rest of the observables we have noticed discrepancies. Also, here in a couple of observables, we see the predicted values are lower than and have opposite signs, and the rest are higher than SM. Therefore, once we have a precise measurements of all these observables, a comparative study will be helpful to distinguish these three type of scenarios.

In addition, we have studied the q^2 distributions of all the asymmetric and angular observables in the two operator scenarios and presented them in fig. 7. These distributions will be helpful to test the NP sensitivities specific to the q^2 regions, which are otherwise missing in the q^2 integrated observables and can be compared with the measurements in small bins in the near future. We have taken the numerical values of the WCs from our fit results of two operator scenarios given

in table 12. As obtained in table 13, we note sizeable NP effects in the observables only for the scenarios $[\mathcal{O}_{S_1}, \mathcal{O}_{S_2}]$, $[\mathcal{O}_{S_2}, \mathcal{O}_T]$ and $[\mathcal{O}_{V_1}, \mathcal{O}_{V_2}]$, respectively. In the items below, we will point out a few important observations from these results.

- All the observables listed above are sensitive to the scenario $[\mathcal{O}_{S_2}, \mathcal{O}_T]$. Interestingly, the q^2 integrated $A_{FB}^{\Lambda_c \tau}$ are consistent with the SM. However, we can see from the respective figure 7 that the corresponding NP predictions have discrepancies with SM in both the high and low q^2 regions. The predicted values throughout the q^2 regions are minimal. The SM predictions are negative in the high- q^2 regions and positive in the low- q^2 regions. Hence, due to a relative cancellation, the q^2 integrated value becomes very small and consistent with the respective NP prediction.
- In the scenario $[\mathcal{O}_{S_2}, \mathcal{O}_T]$ the predictions for $A_{FB}^{\Lambda_c}$, P_{Λ_c} , \hat{K}_{2ss} , \hat{K}_{2cc} , \hat{K}_{3sc} and \hat{K}_{3s} are very small and consistent with zero. The respective SM predictions are either positive or negative and deviate from the NP predictions.
- In the scenario $[\mathcal{O}_{V_1}, \mathcal{O}_{V_2}]$, the predictions for $A_{FB}^{\Lambda_c}$, P_{Λ_c} , \hat{K}_{2ss} , \hat{K}_{2cc} and \hat{K}_{3sc} have opposite sign of the respective SM predictions. These effects can be clearly distinguished from the effects of the $[\mathcal{O}_{S_2}, \mathcal{O}_T]$.
- The predictions of $A_{FB}^{\Lambda_c}$ in the scenarios $[\mathcal{O}_{V_1}, \mathcal{O}_{V_2}]$ and $[\mathcal{O}_{S_2}, \mathcal{O}_T]$ have opposite sign. Also, it is possible to distinguish the effects of these operators in $A_{FB}^{\Lambda_c \tau}$ and \hat{K}_{3s} .
- If the measurements show deviations only in C_F^T , \hat{K}_{1cc} and \hat{K}_{1ss} this could be an indication for contributions from $[\mathcal{O}_{S_2}, \mathcal{O}_T]$. Also, in this scenario in the high- q^2 regions, the prediction of $P_\tau^{(\Lambda_c)}$ has an opposite sign than SM, which is not the case in any other scenario.
- The operator $[\mathcal{O}_{S_1}, \mathcal{O}_{S_2}]$ have significant contributions only in $A_{FB}^{\Lambda_c \tau}$, A_{FB}^T , $P_\tau^{(\Lambda_c)}$ and \hat{K}_{3s} which may be difficult to separate from the effect of either $[\mathcal{O}_{S_2}, \mathcal{O}_T]$ or $[\mathcal{O}_{V_1}, \mathcal{O}_{V_2}]$. However, the scenarios $[\mathcal{O}_{S_2}, \mathcal{O}_T]$ or $[\mathcal{O}_{V_1}, \mathcal{O}_{V_2}]$ have significant contributions in other observables which are distinguishable from each other and from $[\mathcal{O}_{S_1}, \mathcal{O}_{S_2}]$.
- In the observable $P_\tau^{(\Lambda_c)}$, for the scenario $[\mathcal{O}_{S_1}, \mathcal{O}_{S_2}]$, we see the sizeable contribution in the low and high- q^2 regions which are distinguishable from the SM. However, this information is missing in the q^2 integrated prediction since in the high- q^2 , the predicted value is lower than the SM, and in the low- q^2 regions, the prediction is higher than the SM.

The information is available in table 15, 13 and in fig. 7 clearly show that the effects of the two operator scenarios are distinguishable from each other once we have measurements of all the observables mentioned above. Also, suppose there are discrepancies in a few or/a couple of observables. In that case, the pattern of the discrepancies will help distinguish the effects of the one-operator scenario from that of two-operator scenarios.

Finally, we would like to comment on the observables \hat{K}_{4s} and \hat{K}_{4sc} . We can see from the respective expressions in eqns. 8.24 and 8.25 in the appendix that these observables are sensitive to the imaginary components of the helicity amplitudes or to the complex WCs. The values of \hat{K}_{4s} and \hat{K}_{4sc} will be zero if the imaginary part of the relevant WC is zero. Also, we can obtain non-zero contributions in both these observables only in the one operator scenarios \mathcal{O}_{V_1} , \mathcal{O}_{V_2} and \mathcal{O}_T , respectively, with complex WCs. The contributions from the scalar or pseudoscalar operators will always appear in combinations with the other operators. Therefore, these operators with complex WCs in combination with vector, axial-vector and tensor operators can contribute to \hat{K}_{4s} and \hat{K}_{4sc} . In this analysis, we are not considering complex WCs; hence, we have not presented any numerical analysis. We are leaving it for dedicated future work.

6 Summary

We have found the analytical expressions for various asymmetric and angular observables from the angular analysis of $\Lambda_b \rightarrow \Lambda_c^+(\rightarrow \Lambda\pi)\mu^-\bar{\nu}$ and $\Lambda_b \rightarrow \Lambda_c^+(\rightarrow \Lambda\pi)\tau^-\bar{\nu}$ decays in the SM and the NP scenarios. Wherever available, we have compared our analytical expressions with the literature. Using the available lattice inputs on the form factors, we have predicted all these observables alongside the decay rates and LFU ratio $R(\Lambda_c)$ integrated over the whole q^2 regions and small q^2 bins.

Using the available data on $B \rightarrow D^{(*)}\ell^-\bar{\nu}$ decays and $R(\Lambda_c)$, we have extracted the new Wilson coefficients and noticed that only the C_{S_2}, C_{V_2} one operator scenario can explain all these data simultaneously within 3σ . In our operator scenarios, we have predicted all the observables mentioned above and tested their NP sensitivities using our results of the fit. The observation of one operator scenario motivated us to look for two scenarios. We have done the fits to data using two different operator scenarios and found that scenario $[\mathcal{O}_{S_2}, \mathcal{O}_T]$ is the only two operator scenarios which could accommodate comfortably all the measured data simultaneously. In the other two operator scenarios, apart from $R(D^*)$, we are able to explain all the other data simultaneously if we take the uncertainties of our predictions at the 3σ level. We have studied the interesting correlations between the observables in different NP scenarios. In addition, we have studied the NP sensitivities of all the angular and asymmetric observables in all the two operator scenarios and found that many of them show distinguishable sensitivity to the operators $[\mathcal{O}_{S_2}, \mathcal{O}_T]$, $[\mathcal{O}_{V_1}, \mathcal{O}_{V_2}]$ and $[\mathcal{O}_{S_1}, \mathcal{O}_{S_2}]$. Also, the effects of one-operator scenarios are distinguishable from those of two-operator scenarios in these observables.

7 Acknowledgments

RS acknowledges the financial support from the Science and Engineering Research Board (SERB) for the National PostDoctoral Fellowship (file no. NPDF/PDF/2021/003328). SS acknowledges the Council of Scientific and Industrial Research (CSIR), Govt. of India for JRF fellowship grant with File No. 09/731(0173)/2019-EMR-I.

8 Appendix

8.1 Kinematics in Hadronic rest frame and Hadronic matrix elements

$$\begin{aligned} \langle \Lambda_c | \bar{c}\gamma^\mu b | \Lambda_b \rangle &= \bar{u}_{\Lambda_c} \left[f_0(q^2)(m_{\Lambda_b} - m_{\Lambda_c}) \frac{q^\mu}{q^2} + f_+(q^2) \frac{m_{\Lambda_b} + m_{\Lambda_c}}{Q_+} (p_{\Lambda_b}^\mu + p_{\Lambda_c}^\mu - (m_{\Lambda_b}^2 - m_{\Lambda_c}^2) \frac{q^\mu}{q^2}) \right. \\ &\quad \left. + f_\perp(q^2) \left(\gamma^\mu - \frac{2m_{\Lambda_c}}{Q_+} p_{\Lambda_b}^\mu - \frac{2m_{\Lambda_b}}{Q_+} p_{\Lambda_c}^\mu \right) \right] u_{\Lambda_b}, \end{aligned} \quad (8.1)$$

$$\begin{aligned} \langle \Lambda_c | \bar{c}\gamma^\mu \gamma_5 b | \Lambda_b \rangle &= -\bar{u}_{\Lambda_c} \gamma_5 \left[g_0(q^2)(m_{\Lambda_b} + m_{\Lambda_c}) \frac{q^\mu}{q^2} \right. \\ &\quad \left. + g_+(q^2) \frac{m_{\Lambda_b} - m_{\Lambda_c}}{Q_-} (p_{\Lambda_b}^\mu + p_{\Lambda_c}^\mu - (m_{\Lambda_b}^2 - m_{\Lambda_c}^2) \frac{q^\mu}{q^2}) \right. \\ &\quad \left. + g_\perp(q^2) \left(\gamma^\mu + \frac{2m_{\Lambda_c}}{Q_-} p_{\Lambda_b}^\mu - \frac{2m_{\Lambda_b}}{Q_-} p_{\Lambda_c}^\mu \right) \right] u_{\Lambda_b}. \end{aligned} \quad (8.2)$$

The matrix elements of the scalar and pseudo-scalar currents can be obtained from the vector and axial vector matrix elements using the equations of motion:

$$\langle \Lambda_c | \bar{c}b | \Lambda_b \rangle = \frac{q_\mu}{m_b - m_c} \langle \Lambda_c | \bar{c}\gamma^\mu b | \Lambda_b \rangle$$

$$= f_0(q^2) \frac{m_{\Lambda_b} - m_{\Lambda_c}}{m_b - m_c} \bar{u}_{\Lambda_c} u_{\Lambda_b}, \quad (8.3)$$

$$\begin{aligned} \langle \Lambda_c | \bar{c} \gamma_5 b | \Lambda_b \rangle &= \frac{q_\mu}{m_b + m_c} \langle \Lambda_c | \bar{c} \gamma^\mu \gamma_5 b | \Lambda_b \rangle \\ &= g_0(q^2) \frac{m_{\Lambda_b} + m_{\Lambda_c}}{m_b + m_c} \bar{u}_{\Lambda_c} \gamma_5 u_{\Lambda_b}. \end{aligned} \quad (8.4)$$

In our numerical analysis, we use $m_b = 4.18(4)$ GeV, $m_c = 1.27(3)$ GeV [56]. The matrix elements of the tensor currents can be written in terms of four form factors h_+ , h_\perp , \tilde{h}_+ , \tilde{h}_\perp ,

$$\begin{aligned} \langle \Lambda_c | \bar{c} i \sigma^{\mu\nu} b | \Lambda_b \rangle &= \bar{u}_{\Lambda_c} \left[2h_+(q^2) \frac{p_{\Lambda_b}^\mu p_{\Lambda_c}^\nu - p_{\Lambda_b}^\nu p_{\Lambda_c}^\mu}{Q_+} \right. \\ &\quad + h_\perp(q^2) \left(\frac{m_{\Lambda_b} + m_{\Lambda_c}}{q^2} (q^\mu \gamma^\nu - q^\nu \gamma^\mu) - 2 \left(\frac{1}{q^2} + \frac{1}{Q_+} \right) (p_{\Lambda_b}^\mu p_{\Lambda_c}^\nu - p_{\Lambda_b}^\nu p_{\Lambda_c}^\mu) \right) \\ &\quad + \tilde{h}_+(q^2) \left(i \sigma^{\mu\nu} - \frac{2}{Q_-} (m_{\Lambda_b} (p_{\Lambda_c}^\mu \gamma^\nu - p_{\Lambda_c}^\nu \gamma^\mu) \right. \\ &\quad \left. - m_{\Lambda_c} (p_{\Lambda_b}^\mu \gamma^\nu - p_{\Lambda_b}^\nu \gamma^\mu) + p_{\Lambda_b}^\mu p_{\Lambda_c}^\nu - p_{\Lambda_b}^\nu p_{\Lambda_c}^\mu) \right) \\ &\quad + \tilde{h}_\perp(q^2) \frac{m_{\Lambda_b} - m_{\Lambda_c}}{q^2 Q_-} \left((m_{\Lambda_b}^2 - m_{\Lambda_c}^2 - q^2) (\gamma^\mu p_{\Lambda_b}^\nu - \gamma^\nu p_{\Lambda_b}^\mu) \right. \\ &\quad \left. - (m_{\Lambda_b}^2 - m_{\Lambda_c}^2 + q^2) (\gamma^\mu p_{\Lambda_c}^\nu - \gamma^\nu p_{\Lambda_c}^\mu) + 2(m_{\Lambda_b} - m_{\Lambda_c}) (p_{\Lambda_b}^\mu p_{\Lambda_c}^\nu - p_{\Lambda_b}^\nu p_{\Lambda_c}^\mu) \right) \Big] u_{\Lambda_b}. \end{aligned} \quad (8.5)$$

The matrix elements of the current $\bar{c} i \sigma^{\mu\nu} \gamma_5 b$ can be obtained from the above equation by using the identity

$$\sigma^{\mu\nu} \gamma_5 = -\frac{i}{2} \epsilon^{\mu\nu\alpha\beta} \sigma_{\alpha\beta}. \quad (8.6)$$

8.2 Kinematics in leptonic frame and spinor representation

The polarization vectors of the virtual vector boson in this frame are

$$\begin{aligned} \epsilon^{\mu*}(t) &= (1; 0, 0, 0), \\ \epsilon^{\mu*}(\pm 1) &= \frac{1}{\sqrt{2}} (0; \pm 1, -i, 0), \\ \epsilon^{\mu*}(0) &= (0; 0, 0, -1). \end{aligned} \quad (8.7)$$

The three-momentum and energy of the τ lepton in this frame can be written as

$$\begin{aligned} |\mathbf{p}_\tau| &= \sqrt{q^2} v^2/2, \\ E_\tau &= |\mathbf{p}_\tau| + m_\tau^2/\sqrt{q^2}, \end{aligned} \quad (8.8)$$

The lepton spinors for \mathbf{p}_τ pointing in the $+z$ direction and $\mathbf{p}_{\bar{\nu}_\tau}$ pointing in the $-z$ direction are

The Leptonic three momentum p_τ along any arbitrary direction $p_\tau(\theta, \phi)$ with polar angle θ , and azimuthal angle ϕ calculated as follow

$$\begin{aligned} \bar{u}_\tau(+\frac{1}{2}, p_\tau) &= \sqrt{E_\tau + m_\tau} \left(\cos(\theta_\tau/2), \sin(\theta_\tau/2), \frac{-|\mathbf{p}_\tau|}{E_\tau + m_\tau} \cos(\theta_\tau/2), \frac{-|\mathbf{p}_\tau|}{E_\tau + m_\tau} \sin(\theta_\tau/2) \right), \\ \bar{u}_\tau(-\frac{1}{2}, p_\tau) &= \sqrt{E_\tau + m_\tau} \left(-\sin(\theta_\tau/2), \cos(\theta_\tau/2), \frac{-|\mathbf{p}_\tau|}{E_\tau + m_\tau} \sin(\theta_\tau/2), \frac{|\mathbf{p}_\tau|}{E_\tau + m_\tau} \cos(\theta_\tau/2) \right), \\ v_{\bar{\nu}_\tau}(\frac{1}{2}, p_{\bar{\nu}_\tau}) &= \sqrt{E_\nu} \left(\cos(\theta_\tau/2) \quad \sin(\theta_\tau/2) \quad -\cos(\theta_\tau/2) \quad -\sin(\theta_\tau/2) \right)^T. \end{aligned} \quad (8.9)$$

8.2.1 Hadronic Couplings in $\Lambda_c^+ \rightarrow \Lambda\pi^+$

In the SM the decay $\Lambda_c^+ \rightarrow \Lambda\pi^+$ is described by the effective Hamiltonian

$$H_{\Delta S=1}^{\text{eff}} = \frac{4G_F}{\sqrt{2}} V_{ud}^* V_{us} [\bar{d}\gamma_\mu P_L u] [\bar{s}\gamma^\mu P_L c]. \quad (8.10)$$

The hadronic matrix element which determines the $\Lambda_c \rightarrow \Lambda\pi$ decay can be parametrized as

$$\begin{aligned} & \langle \Lambda(k_1, \lambda_\Lambda) \pi^+(k_2) | [\bar{d}\gamma_\mu P_L u] [\bar{s}\gamma^\mu P_L c] | \Lambda(k, \lambda_{\Lambda_c}) \rangle \\ &= [\bar{u}(k_1, \lambda_\Lambda) (\xi \gamma_5 + \omega) u(k, \lambda_{\Lambda_c})] \equiv \mathcal{A}_{\lambda_\Lambda}^{\lambda_{\Lambda_c}}. \end{aligned} \quad (8.11)$$

As a consequence of the equations of motion, only two independent hadronic parameters appear which we have denoted as ξ and ω . They can be extracted from the $\Lambda_c^+ \rightarrow \Lambda\pi^+$ decay width and polarization measurements.

In terms of the kinematic variables introduced above, the helicity amplitudes for the secondary decay can be written as

$$\begin{aligned} \mathcal{A}_{+1/2}^{+1/2} &= (\sqrt{r_+} \omega - \sqrt{r_-} \xi) \cos \frac{\theta_\Lambda}{2}, \\ \mathcal{A}_{-1/2}^{+1/2} &= (\sqrt{r_+} \omega + \sqrt{r_-} \xi) \sin \frac{\theta_\Lambda}{2} e^{i\phi}, \\ \mathcal{A}_{+1/2}^{-1/2} &= (-\sqrt{r_+} \omega + \sqrt{r_-} \xi) \sin \frac{\theta_\Lambda}{2} e^{-i\phi}, \\ \mathcal{A}_{-1/2}^{-1/2} &= (\sqrt{r_+} \omega + \sqrt{r_-} \xi) \cos \frac{\theta_\Lambda}{2}. \end{aligned} \quad (8.12)$$

where we abbreviate

$$r_\pm \equiv (m_{\Lambda_c} \pm m_\Lambda)^2 - m_\pi^2. \quad (8.13)$$

Here the $\Lambda_c \rightarrow \Lambda\pi$ decay width is given as

$$\Gamma_\Lambda = \frac{|N_2|^2 \sqrt{r_+ r_-}}{16\pi m_\Lambda^3} (r_- |\xi|^2 + r_+ |\omega|^2), \quad (8.14)$$

with $N_2 = \frac{4G_F}{\sqrt{2}} V_{ud}^* V_{us}$. and the parity-violating decay parameter α_Λ reads

$$\alpha_\Lambda = \frac{-2re[\omega\xi]}{\sqrt{\frac{r_-}{r_+} |\xi|^2 + \sqrt{\frac{r_+}{r_-}} |\omega|^2}} = +\alpha^{\text{exp}_\Lambda}. \quad (8.15)$$

8.3 Explicit expression for Angular Observables

$$\begin{aligned} K_{1c} = & N \left[2 \left(|H_{\frac{1}{2},+1}^{\text{VA}}|^2 - |H_{-\frac{1}{2},-1}^{\text{VA}}|^2 \right) + 8 \operatorname{Re} \left[H_{\frac{1}{2},0}^{\text{SP}*} H_{\frac{1}{2},t,0}^{T,\frac{1}{2}} + H_{-\frac{1}{2},0}^{\text{SP}*} H_{-\frac{1}{2},t,0}^{T,-\frac{1}{2}} - H_{-\frac{1}{2},0}^{\text{SP}*} H_{-\frac{1}{2},+1,-1}^{T,-\frac{1}{2}} - H_{\frac{1}{2},0}^{\text{SP}*} H_{\frac{1}{2},+1,-1}^{T,\frac{1}{2}} \right] \right. \\ & + \frac{m_\ell}{\sqrt{q^2}} \left\{ \operatorname{Re} \left[4H_{-\frac{1}{2},0}^{\text{SP}*} H_{-\frac{1}{2},0}^{\text{VA}} + 4H_{\frac{1}{2},0}^{\text{SP}*} H_{\frac{1}{2},0}^{\text{VA}} + 8 \left(H_{\frac{1}{2},+1}^{\text{VA}*} H_{\frac{1}{2},t,1}^{T,-\frac{1}{2}} + H_{-\frac{1}{2},t,0}^{T,-\frac{1}{2}} H_{-\frac{1}{2},t}^{\text{VA}*} + H_{\frac{1}{2},t,0}^{T,\frac{1}{2}} H_{\frac{1}{2},t}^{\text{VA}*} \right. \right. \right. \\ & \left. \left. - H_{-\frac{1}{2},-1,0}^{T,\frac{1}{2}} H_{-\frac{1}{2},-1}^{\text{VA}*} - H_{\frac{1}{2},+1,0}^{T,-\frac{1}{2}} H_{\frac{1}{2},+1}^{\text{VA}*} - H_{-\frac{1}{2},+1,-1}^{T,-\frac{1}{2}} H_{-\frac{1}{2},t}^{\text{VA}*} - H_{\frac{1}{2},+1,-1}^{T,\frac{1}{2}} H_{\frac{1}{2},t}^{\text{VA}*} - H_{-\frac{1}{2},-1}^{\text{VA}*} H_{-\frac{1}{2},t,-1}^{T,\frac{1}{2}} \right) \right] \left. \right\} \\ & + \frac{m_\ell^2}{q^2} \left\{ 8 \left(|H_{\frac{1}{2},+1,0}^{T,-\frac{1}{2}}|^2 - |H_{-\frac{1}{2},-1,0}^{T,\frac{1}{2}}|^2 - |H_{-\frac{1}{2},t,-1}^{T,\frac{1}{2}}|^2 + |H_{\frac{1}{2},t,+1}^{T,-\frac{1}{2}}|^2 \right) \right. \\ & \left. + \operatorname{Re} \left[4H_{-\frac{1}{2},0}^{\text{VA}*} H_{-\frac{1}{2},t}^{\text{VA}} + 4H_{\frac{1}{2},0}^{\text{VA}*} H_{\frac{1}{2},t}^{\text{VA}} - 16H_{-\frac{1}{2},-1,0}^{T,\frac{1}{2}*} H_{-\frac{1}{2},t,-1}^{T,\frac{1}{2}} - 16H_{\frac{1}{2},+1,0}^{T,-\frac{1}{2}*} H_{\frac{1}{2},t,1}^{T,-\frac{1}{2}} \right] \right\} \quad (8.16) \end{aligned}$$

$$\begin{aligned}
K_{1cc} = & N \left[2 \left(|H_{-\frac{1}{2},0}^{\text{SP}}|^2 + |H_{\frac{1}{2},0}^{\text{SP}}|^2 + |H_{-\frac{1}{2},-1}^{\text{VA}}|^2 + |H_{\frac{1}{2},+1}^{\text{VA}}|^2 \right) \right. \\
& + 8 \left(|H_{-\frac{1}{2},+1,-1}^{T,-\frac{1}{2}}|^2 + |H_{\frac{1}{2},+1,-1}^{T,\frac{1}{2}}|^2 + |H_{-\frac{1}{2},t,0}^{T,-\frac{1}{2}}|^2 + |H_{\frac{1}{2},t,0}^{T,\frac{1}{2}}|^2 \right) \\
& - 16 \text{Re} \left[H_{-\frac{1}{2},+1,-1}^{T,-\frac{1}{2}*} H_{-\frac{1}{2},t,0}^{T,-\frac{1}{2}} + H_{\frac{1}{2},+1,-1}^{T,\frac{1}{2}*} H_{\frac{1}{2},t,0}^{T,\frac{1}{2}} \right] \\
& + \frac{m_\ell}{\sqrt{q^2}} \left\{ \text{Re} \left[4 \left(H_{-\frac{1}{2},0}^{\text{SP}*} H_{-\frac{1}{2},t}^{\text{VA}} + H_{\frac{1}{2},0}^{\text{SP}*} H_{\frac{1}{2},t}^{\text{VA}} \right) \right. \right. \\
& + 8 \left(H_{-\frac{1}{2},0}^{\text{VA}*} H_{-\frac{1}{2},t,0}^{T,-\frac{1}{2}} - H_{-\frac{1}{2},0}^{\text{VA}*} H_{-\frac{1}{2},+1,-1}^{T,-\frac{1}{2}} - H_{\frac{1}{2},0}^{\text{VA}*} H_{\frac{1}{2},+1,-1}^{T,\frac{1}{2}} + H_{\frac{1}{2},0}^{\text{VA}*} H_{\frac{1}{2},t,0}^{T,\frac{1}{2}} \right. \\
& + H_{-\frac{1}{2},-1,0}^{T,\frac{1}{2}} H_{-\frac{1}{2},-1}^{\text{VA}*} - H_{\frac{1}{2},+1,0}^{T,-\frac{1}{2}} H_{\frac{1}{2},+1}^{\text{VA}*} + H_{-\frac{1}{2},-1}^{\text{VA}*} H_{-\frac{1}{2},t,-1}^{T,\frac{1}{2}} + H_{\frac{1}{2},+1}^{\text{VA}*} H_{\frac{1}{2},t,1}^{T,-\frac{1}{2}} \left. \left. \right] \right\} \\
& + \frac{m_\ell^2}{q^2} \left\{ 2 \left(|H_{-\frac{1}{2},0}^{\text{VA}}|^2 + |H_{\frac{1}{2},0}^{\text{VA}}|^2 + |H_{-\frac{1}{2},t}^{\text{VA}}|^2 + |H_{\frac{1}{2},t}^{\text{VA}}|^2 \right) \right. \\
& + 8 \left(|H_{-\frac{1}{2},-1,0}^{T,\frac{1}{2}}|^2 + |H_{\frac{1}{2},+1,0}^{T,-\frac{1}{2}}|^2 + |H_{-\frac{1}{2},t,-1}^{T,\frac{1}{2}}|^2 + |H_{\frac{1}{2},t,+1}^{T,-\frac{1}{2}}|^2 \right) \\
& \left. + 16 \text{Re} \left[H_{-\frac{1}{2},-1,0}^{T,\frac{1}{2}*} H_{-\frac{1}{2},t,-1}^{T,\frac{1}{2}} - H_{\frac{1}{2},+1,0}^{T,-\frac{1}{2}*} H_{\frac{1}{2},t,1}^{T,-\frac{1}{2}} \right] \right\} \quad (8.17)
\end{aligned}$$

$$\begin{aligned}
K_{1ss} = & N \left[|H_{-\frac{1}{2},-1}^{\text{VA}}|^2 + |H_{\frac{1}{2},+1}^{\text{VA}}|^2 + 2 \left(|H_{\frac{1}{2},0}^{\text{SP}}|^2 + |H_{-\frac{1}{2},0}^{\text{SP}}|^2 + |H_{-\frac{1}{2},0}^{\text{VA}}|^2 + |H_{\frac{1}{2},0}^{\text{VA}}|^2 \right) \right. \\
& + 4 \left(|H_{\frac{1}{2},+1,0}^{T,-\frac{1}{2}}|^2 + |H_{-\frac{1}{2},-1,0}^{T,\frac{1}{2}}|^2 + |H_{-\frac{1}{2},t,-1}^{T,\frac{1}{2}}|^2 + |H_{\frac{1}{2},t,+1}^{T,-\frac{1}{2}}|^2 \right) + 8 \text{Re} \left[H_{-\frac{1}{2},-1,0}^{T,\frac{1}{2}*} H_{-\frac{1}{2},t,-1}^{T,\frac{1}{2}} - H_{\frac{1}{2},+1,0}^{T,-\frac{1}{2}*} H_{\frac{1}{2},t,1}^{T,-\frac{1}{2}} \right] \\
& + \frac{m_\ell}{\sqrt{q^2}} \left\{ 4 \text{Re} \left[H_{-\frac{1}{2},0}^{\text{SP}*} H_{-\frac{1}{2},t}^{\text{VA}} + H_{\frac{1}{2},0}^{\text{SP}*} H_{\frac{1}{2},t}^{\text{VA}} \right] \right. \\
& + 8 \text{Re} \left[H_{-\frac{1}{2},0}^{\text{VA}*} H_{-\frac{1}{2},t,0}^{T,-\frac{1}{2}} - H_{-\frac{1}{2},0}^{\text{VA}*} H_{-\frac{1}{2},+1,-1}^{T,-\frac{1}{2}} - H_{\frac{1}{2},0}^{\text{VA}*} H_{\frac{1}{2},+1,-1}^{T,\frac{1}{2}} \right. \\
& + H_{\frac{1}{2},0}^{\text{VA}*} H_{\frac{1}{2},t,0}^{T,\frac{1}{2}} + H_{-\frac{1}{2},-1,0}^{T,\frac{1}{2}} H_{-\frac{1}{2},-1}^{\text{VA}*} - H_{\frac{1}{2},+1,0}^{T,-\frac{1}{2}} H_{\frac{1}{2},+1}^{\text{VA}*} \\
& \left. \left. + H_{-\frac{1}{2},-1}^{\text{VA}*} H_{-\frac{1}{2},t,-1}^{T,\frac{1}{2}} + H_{\frac{1}{2},+1}^{\text{VA}*} H_{\frac{1}{2},t,1}^{T,-\frac{1}{2}} \right] \right\} \\
& + \frac{m_\ell^2}{q^2} \left\{ |H_{-\frac{1}{2},-1}^{\text{VA}}|^2 + |H_{\frac{1}{2},+1}^{\text{VA}}|^2 + 2 \left(|H_{-\frac{1}{2},t}^{\text{VA}}|^2 + |H_{\frac{1}{2},t}^{\text{VA}}|^2 \right) \right. \\
& + 4 \left(|H_{-\frac{1}{2},-1,0}^{T,\frac{1}{2}}|^2 + |H_{\frac{1}{2},+1,0}^{T,-\frac{1}{2}}|^2 + |H_{-\frac{1}{2},t,-1}^{T,\frac{1}{2}}|^2 + |H_{\frac{1}{2},t,+1}^{T,-\frac{1}{2}}|^2 \right) \\
& + 8 \left(|H_{-\frac{1}{2},+1,-1}^{T,-\frac{1}{2}}|^2 + |H_{\frac{1}{2},+1,-1}^{T,\frac{1}{2}}|^2 + |H_{-\frac{1}{2},t,0}^{T,-\frac{1}{2}}|^2 + |H_{\frac{1}{2},t,0}^{T,\frac{1}{2}}|^2 \right) \\
& \left. + 8 \text{Re} \left[H_{-\frac{1}{2},-1,0}^{T,\frac{1}{2}*} H_{-\frac{1}{2},t,-1}^{T,\frac{1}{2}} - H_{\frac{1}{2},+1,0}^{T,-\frac{1}{2}*} H_{\frac{1}{2},t,1}^{T,-\frac{1}{2}} - 2H_{-\frac{1}{2},+1,-1}^{T,-\frac{1}{2}*} H_{-\frac{1}{2},t,0}^{T,-\frac{1}{2}} - 2H_{\frac{1}{2},+1,-1}^{T,\frac{1}{2}*} H_{\frac{1}{2},t,0}^{T,\frac{1}{2}} \right] \right\} \quad (8.18)
\end{aligned}$$

$$\begin{aligned}
K_{2c} = & N \alpha_\Lambda \left[2 \left\{ |H_{-\frac{1}{2},-1}^{\text{VA}}|^2 + |H_{\frac{1}{2},+1}^{\text{VA}}|^2 + 4 \text{Re} \left[H_{-\frac{1}{2},0}^{\text{SP}*} H_{-\frac{1}{2},+1,-1}^{T,-\frac{1}{2}} - H_{\frac{1}{2},0}^{\text{SP}*} H_{\frac{1}{2},+1,-1}^{T,\frac{1}{2}} - H_{-\frac{1}{2},0}^{\text{SP}*} H_{-\frac{1}{2},t,0}^{T,-\frac{1}{2}} + H_{\frac{1}{2},0}^{\text{SP}*} H_{\frac{1}{2},t,0}^{T,\frac{1}{2}} \right] \right\} \right. \\
& \left. - \frac{4m_\ell}{\sqrt{q^2}} \left\{ \text{Re} \left[H_{-\frac{1}{2},0}^{\text{SP}*} H_{-\frac{1}{2},0}^{\text{VA}} - H_{\frac{1}{2},0}^{\text{SP}*} H_{\frac{1}{2},0}^{\text{VA}} - 2H_{-\frac{1}{2},-1,0}^{T,\frac{1}{2}} H_{-\frac{1}{2},-1}^{\text{VA}*} + 2H_{\frac{1}{2},+1,0}^{T,-\frac{1}{2}} H_{\frac{1}{2},+1}^{\text{VA}*} - 2H_{-\frac{1}{2},+1,-1}^{T,-\frac{1}{2}} H_{-\frac{1}{2},t}^{\text{VA}*} \right] \right\} \right.
\end{aligned}$$

$$\begin{aligned}
& + 2H_{\frac{1}{2},+1,-1}^{T,\frac{1}{2}} H_{\frac{1}{2},t}^{\text{VA}*} - 2H_{-\frac{1}{2},-1}^{\text{VA}*} H_{-\frac{1}{2},t,-1}^{T,\frac{1}{2}} - 2H_{\frac{1}{2},+1}^{\text{VA}*} H_{\frac{1}{2},t,1}^{T,-\frac{1}{2}} + 2H_{-\frac{1}{2},t,0}^{T,-\frac{1}{2}} H_{-\frac{1}{2},t}^{\text{VA}*} - 2H_{\frac{1}{2},t,0}^{T,\frac{1}{2}} H_{\frac{1}{2},t}^{\text{VA}*} \Big] \Big\} \\
& + \frac{4m_\ell^2}{q^2} \left\{ \text{Re} \left[2|H_{-\frac{1}{2},-1,0}^{T,\frac{1}{2}}|^2 + 2|H_{\frac{1}{2},+1,0}^{T,-\frac{1}{2}}|^2 + 2|H_{-\frac{1}{2},t,-1}^{T,\frac{1}{2}}|^2 + 2|H_{\frac{1}{2},t,+1}^{T,-\frac{1}{2}}|^2 \right. \right. \\
& \left. \left. + H_{\frac{1}{2},0}^{\text{VA}*} H_{\frac{1}{2},t}^{\text{VA}} - H_{-\frac{1}{2},0}^{\text{VA}*} H_{-\frac{1}{2},t}^{\text{VA}} + 4H_{-\frac{1}{2},-1,0}^{T,\frac{1}{2}*} H_{-\frac{1}{2},t,-1}^{T,\frac{1}{2}} - 4H_{\frac{1}{2},+1,0}^{T,-\frac{1}{2}*} H_{\frac{1}{2},t,1}^{T,-\frac{1}{2}} \right] \right\} \quad (8.19)
\end{aligned}$$

$$\begin{aligned}
K_{2cc} = & -\alpha_\Lambda N \left[2 \left\{ |H_{-\frac{1}{2},0}^{\text{SP}}|^2 - |H_{\frac{1}{2},0}^{\text{SP}}|^2 + |H_{-\frac{1}{2},-1}^{\text{VA}}|^2 - |H_{\frac{1}{2},+1}^{\text{VA}}|^2 \right. \right. \\
& + 4|H_{-\frac{1}{2},+1,-1}^{T,-\frac{1}{2}}|^2 - 4|H_{\frac{1}{2},+1,-1}^{T,\frac{1}{2}}|^2 + 4|H_{-\frac{1}{2},t,0}^{T,-\frac{1}{2}}|^2 - 4|H_{\frac{1}{2},t,0}^{T,\frac{1}{2}}|^2 \\
& \left. - 8 \text{Re} \left[H_{-\frac{1}{2},+1,-1}^{T,-\frac{1}{2}*} H_{-\frac{1}{2},t,0}^{T,-\frac{1}{2}} - H_{\frac{1}{2},+1,-1}^{T,\frac{1}{2}*} H_{\frac{1}{2},t,0}^{T,\frac{1}{2}} \right] \right\} \\
& + \frac{4m_\ell}{\sqrt{q^2}} \left\{ \text{Re} \left[H_{-\frac{1}{2},0}^{\text{SP}*} H_{-\frac{1}{2},t}^{\text{VA}} - H_{\frac{1}{2},0}^{\text{SP}*} H_{\frac{1}{2},t}^{\text{VA}} - 2H_{-\frac{1}{2},0}^{\text{VA}*} H_{-\frac{1}{2},+1,-1}^{T,-\frac{1}{2}} + 2H_{-\frac{1}{2},0}^{\text{VA}*} H_{-\frac{1}{2},t,0}^{T,-\frac{1}{2}} \right. \right. \\
& + 2H_{\frac{1}{2},0}^{\text{VA}*} H_{\frac{1}{2},+1,-1}^{T,\frac{1}{2}} - 2H_{\frac{1}{2},0}^{\text{VA}*} H_{\frac{1}{2},t,0}^{T,\frac{1}{2}} \\
& + 2H_{-\frac{1}{2},-1,0}^{T,\frac{1}{2}} H_{-\frac{1}{2},-1}^{\text{VA}*} + 2H_{\frac{1}{2},+1,0}^{T,-\frac{1}{2}} H_{\frac{1}{2},+1}^{\text{VA}*} + 2H_{-\frac{1}{2},-1}^{\text{VA}*} H_{-\frac{1}{2},t,-1}^{T,\frac{1}{2}} - 2H_{\frac{1}{2},+1}^{\text{VA}*} H_{\frac{1}{2},t,+1}^{T,-\frac{1}{2}} \Big] \Big\} \\
& + \frac{2m_\ell^2}{q^2} \left\{ |H_{-\frac{1}{2},0}^{\text{VA}}|^2 - |H_{\frac{1}{2},0}^{\text{VA}}|^2 + |H_{-\frac{1}{2},t}^{\text{VA}}|^2 - |H_{\frac{1}{2},t}^{\text{VA}}|^2 + 4|H_{-\frac{1}{2},-1,0}^{T,\frac{1}{2}}|^2 \right. \\
& \left. - 4|H_{\frac{1}{2},+1,0}^{T,-\frac{1}{2}}|^2 + 4|H_{-\frac{1}{2},t,-1}^{T,\frac{1}{2}}|^2 - 4|H_{\frac{1}{2},t,+1}^{T,-\frac{1}{2}}|^2 + 8 \text{Re} \left[H_{-\frac{1}{2},-1,0}^{T,\frac{1}{2}*} H_{-\frac{1}{2},t,-1}^{T,\frac{1}{2}} + H_{\frac{1}{2},+1,0}^{T,-\frac{1}{2}*} H_{\frac{1}{2},t,+1}^{T,-\frac{1}{2}} \right] \right\} \Big] \quad (8.20)
\end{aligned}$$

$$\begin{aligned}
K_{2ss} = & -\alpha_\Lambda N \left[\left\{ \left(|H_{-\frac{1}{2},-1}^{\text{VA}}|^2 - |H_{\frac{1}{2},+1}^{\text{VA}}|^2 \right) + 2 \left(|H_{-\frac{1}{2},0}^{\text{SP}}|^2 + |H_{-\frac{1}{2},0}^{\text{VA}}|^2 - |H_{\frac{1}{2},0}^{\text{SP}}|^2 - |H_{\frac{1}{2},0}^{\text{VA}}|^2 \right) \right. \right. \\
& + 4 \left(|H_{-\frac{1}{2},-1,0}^{T,\frac{1}{2}}|^2 + |H_{-\frac{1}{2},t,-1}^{T,\frac{1}{2}}|^2 - |H_{\frac{1}{2},+1,0}^{T,-\frac{1}{2}}|^2 - |H_{\frac{1}{2},t,+1}^{T,-\frac{1}{2}}|^2 \right) \\
& \left. + 8 \text{Re} \left[H_{-\frac{1}{2},-1,0}^{T,\frac{1}{2}*} H_{-\frac{1}{2},t,-1}^{T,\frac{1}{2}} + 8H_{\frac{1}{2},+1,0}^{T,-\frac{1}{2}*} H_{\frac{1}{2},t,+1}^{T,-\frac{1}{2}} \right] \right\} \\
& + \frac{4m_\ell}{\sqrt{q^2}} \left\{ \text{Re} \left[H_{-\frac{1}{2},0}^{\text{SP}*} H_{-\frac{1}{2},t}^{\text{VA}} - H_{\frac{1}{2},0}^{\text{SP}*} H_{\frac{1}{2},t}^{\text{VA}} - 2H_{-\frac{1}{2},0}^{\text{VA}*} H_{-\frac{1}{2},+1,-1}^{T,-\frac{1}{2}} + 2H_{-\frac{1}{2},0}^{\text{VA}*} H_{-\frac{1}{2},t,0}^{T,-\frac{1}{2}} + 2H_{\frac{1}{2},0}^{\text{VA}*} H_{\frac{1}{2},+1,-1}^{T,\frac{1}{2}} \right. \right. \\
& \left. \left. - 2H_{\frac{1}{2},0}^{\text{VA}*} H_{\frac{1}{2},t,0}^{T,\frac{1}{2}} + 2H_{-\frac{1}{2},-1,0}^{T,\frac{1}{2}} H_{-\frac{1}{2},-1}^{\text{VA}*} + 2H_{\frac{1}{2},+1,0}^{T,-\frac{1}{2}} H_{\frac{1}{2},+1}^{\text{VA}*} + 2H_{-\frac{1}{2},-1}^{\text{VA}*} H_{-\frac{1}{2},t,-1}^{T,\frac{1}{2}} - 2H_{\frac{1}{2},+1}^{\text{VA}*} H_{\frac{1}{2},t,+1}^{T,-\frac{1}{2}} \right] \right\} \\
& + \frac{m_\ell^2}{q^2} \left\{ |H_{-\frac{1}{2},-1}^{\text{VA}}|^2 - |H_{\frac{1}{2},+1}^{\text{VA}}|^2 + 2|H_{-\frac{1}{2},t}^{\text{VA}}|^2 - 2|H_{\frac{1}{2},t}^{\text{VA}}|^2 \right. \\
& + 4|H_{-\frac{1}{2},t,-1}^{T,\frac{1}{2}}|^2 - 4|H_{\frac{1}{2},t,+1}^{T,-\frac{1}{2}}|^2 + 4|H_{-\frac{1}{2},-1,0}^{T,\frac{1}{2}}|^2 - 4|H_{\frac{1}{2},+1,0}^{T,-\frac{1}{2}}|^2 \\
& + 8|H_{-\frac{1}{2},+1,-1}^{T,-\frac{1}{2}}|^2 - 8|H_{\frac{1}{2},+1,-1}^{T,\frac{1}{2}}|^2 + 8|H_{-\frac{1}{2},t,0}^{T,-\frac{1}{2}}|^2 - 8|H_{\frac{1}{2},t,0}^{T,\frac{1}{2}}|^2 \\
& \left. + 8 \text{Re} \left[H_{-\frac{1}{2},-1,0}^{T,\frac{1}{2}*} H_{-\frac{1}{2},t,-1}^{T,\frac{1}{2}} + 8H_{\frac{1}{2},+1,0}^{T,-\frac{1}{2}*} H_{\frac{1}{2},t,+1}^{T,-\frac{1}{2}} - 16H_{-\frac{1}{2},+1,-1}^{T,-\frac{1}{2}*} H_{-\frac{1}{2},t,0}^{T,-\frac{1}{2}} + 16H_{\frac{1}{2},+1,-1}^{T,\frac{1}{2}*} H_{\frac{1}{2},t,0}^{T,\frac{1}{2}} \right] \right\} \Big] \quad (8.21)
\end{aligned}$$

$$K_{3sc} = -2\sqrt{2}\alpha_\Lambda N \left(1 - \frac{m_\ell^2}{q^2} \right) \times \text{Re} \left[\left(H_{-\frac{1}{2},0}^{\text{VA}*} H_{\frac{1}{2},+1}^{\text{VA}} - H_{\frac{1}{2},0}^{\text{VA}*} H_{-\frac{1}{2},-1}^{\text{VA}} \right) \right]$$

$$- H_{\frac{1}{2},+1,0}^{T,-\frac{1}{2}*} H_{-\frac{1}{2},t,0}^{T,-\frac{1}{2}} + H_{-\frac{1}{2},+1,-1}^{T,-\frac{1}{2}*} H_{\frac{1}{2},t,1}^{T,-\frac{1}{2}} + H_{\frac{1}{2},+1,-1}^{T,\frac{1}{2}*} H_{-\frac{1}{2},t,-1}^{T,\frac{1}{2}} + H_{-\frac{1}{2},t,0}^{T,-\frac{1}{2}} H_{\frac{1}{2},t,1}^{T,-\frac{1}{2}*} - H_{\frac{1}{2},t,0}^{T,\frac{1}{2}*} H_{-\frac{1}{2},t,-1}^{T,\frac{1}{2}} \Big) \Big] \quad (8.25)$$

$$\begin{aligned} \frac{d\Gamma^{\tau=+1/2}}{dq^2} &= \frac{3N}{2} \left[4|H_{-\frac{1}{2},0}^{\text{SP}}|^2 + 4|H_{\frac{1}{2},0}^{\text{SP}}|^2 \right. \\ &+ \frac{16}{3} \left(|H_{-\frac{1}{2},-1,0}^{T,\frac{1}{2}}|^2 + |H_{\frac{1}{2},+1,0}^{T,-\frac{1}{2}}|^2 + |H_{-\frac{1}{2},+1,-1}^{T,-\frac{1}{2}}|^2 + |H_{\frac{1}{2},+1,-1}^{T,\frac{1}{2}}|^2 \right. \\ &+ \left. |H_{-\frac{1}{2},t,0}^{T,-\frac{1}{2}}|^2 + |H_{\frac{1}{2},t,0}^{T,\frac{1}{2}}|^2 + |H_{-\frac{1}{2},t,-1}^{T,\frac{1}{2}}|^2 + |H_{\frac{1}{2},t,+1}^{T,-\frac{1}{2}}|^2 \right) \\ &+ \frac{32}{3} \text{Re} \left[H_{-\frac{1}{2},-1,0}^{T,\frac{1}{2}*} H_{-\frac{1}{2},t,-1}^{T,\frac{1}{2}} - H_{\frac{1}{2},+1,0}^{T,-\frac{1}{2}*} H_{\frac{1}{2},t,+1}^{T,-\frac{1}{2}} - H_{-\frac{1}{2},+1,-1}^{T,-\frac{1}{2}*} H_{-\frac{1}{2},t,0}^{T,-\frac{1}{2}} - H_{\frac{1}{2},+1,-1}^{T,\frac{1}{2}*} H_{\frac{1}{2},t,0}^{T,\frac{1}{2}} \right] \\ &+ \frac{m_\ell}{\sqrt{q^2}} \left\{ 8\text{Re} \left[H_{-\frac{1}{2},0}^{\text{SP}*} H_{-\frac{1}{2},t}^{\text{VA}} + H_{\frac{1}{2},0}^{\text{SP}*} H_{\frac{1}{2},t}^{\text{VA}} \right] \right. \\ &- \frac{16}{3} \left[H_{-\frac{1}{2},0}^{\text{VA}*} H_{-\frac{1}{2},+1,-1}^{T,-\frac{1}{2}} + H_{-\frac{1}{2},0}^{\text{VA}*} H_{-\frac{1}{2},t,0}^{T,-\frac{1}{2}} - H_{\frac{1}{2},0}^{\text{VA}*} H_{\frac{1}{2},+1,-1}^{T,\frac{1}{2}} + H_{\frac{1}{2},0}^{\text{VA}*} H_{\frac{1}{2},t,0}^{T,\frac{1}{2}} + H_{-\frac{1}{2},-1,0}^{T,\frac{1}{2}} H_{-\frac{1}{2},-1}^{\text{VA}*} \right. \\ &- \left. H_{\frac{1}{2},+1,0}^{T,-\frac{1}{2}} H_{\frac{1}{2},+1}^{\text{VA}*} + H_{-\frac{1}{2},-1}^{\text{VA}*} H_{-\frac{1}{2},t,-1}^{T,\frac{1}{2}} + H_{\frac{1}{2},+1}^{\text{VA}*} H_{\frac{1}{2},t,+1}^{T,-\frac{1}{2}} \right] \Big\} \\ &+ \frac{m_\ell^2}{q^2} \left\{ \frac{4}{3} \left(|H_{-\frac{1}{2},0}^{\text{VA}}|^2 + |H_{\frac{1}{2},0}^{\text{VA}}|^2 + |H_{-\frac{1}{2},-1}^{\text{VA}}|^2 + |H_{\frac{1}{2},+1}^{\text{VA}}|^2 \right) + 4|H_{-\frac{1}{2},t}^{\text{VA}}|^2 + 4|H_{\frac{1}{2},t}^{\text{VA}}|^2 \right\} \Big] \quad (8.26) \end{aligned}$$

$$\begin{aligned} \frac{d\Gamma^{\tau=-1/2}}{dq^2} &= \frac{3N}{2} \left[\frac{8}{3} \left(|H_{-\frac{1}{2},0}^{\text{VA}}|^2 + |H_{\frac{1}{2},0}^{\text{VA}}|^2 + |H_{-\frac{1}{2},-1}^{\text{VA}}|^2 + |H_{\frac{1}{2},+1}^{\text{VA}}|^2 \right) \right. \\ &+ \frac{32}{3} \frac{m_\ell}{\sqrt{q^2}} \text{Re} \left[-H_{-\frac{1}{2},0}^{\text{VA}*} H_{-\frac{1}{2},+1,-1}^{T,-\frac{1}{2}} + H_{-\frac{1}{2},0}^{\text{VA}*} H_{-\frac{1}{2},t,0}^{T,-\frac{1}{2}} - H_{\frac{1}{2},0}^{\text{VA}*} H_{\frac{1}{2},+1,-1}^{T,\frac{1}{2}} + H_{\frac{1}{2},0}^{\text{VA}*} H_{\frac{1}{2},t,0}^{T,\frac{1}{2}} + H_{-\frac{1}{2},-1,0}^{T,\frac{1}{2}} H_{-\frac{1}{2},-1}^{\text{VA}*} \right. \\ &- \left. H_{\frac{1}{2},+1,0}^{T,-\frac{1}{2}} H_{\frac{1}{2},+1}^{\text{VA}*} + H_{-\frac{1}{2},-1}^{\text{VA}*} H_{-\frac{1}{2},t,-1}^{T,\frac{1}{2}} + H_{\frac{1}{2},+1}^{\text{VA}*} H_{\frac{1}{2},t,+1}^{T,-\frac{1}{2}} \right] \\ &+ \frac{32}{3} \frac{m_\ell^2}{q^2} \left\{ 2\text{Re} \left[H_{-\frac{1}{2},-1,0}^{T,\frac{1}{2}*} H_{-\frac{1}{2},t,-1}^{T,\frac{1}{2}} - H_{\frac{1}{2},+1,0}^{T,-\frac{1}{2}*} H_{\frac{1}{2},t,+1}^{T,-\frac{1}{2}} - H_{-\frac{1}{2},+1,-1}^{T,-\frac{1}{2}*} H_{-\frac{1}{2},t,0}^{T,-\frac{1}{2}} - H_{\frac{1}{2},+1,-1}^{T,\frac{1}{2}*} H_{\frac{1}{2},t,0}^{T,\frac{1}{2}} \right] \right. \\ &+ \left(|H_{-\frac{1}{2},-1,0}^{T,\frac{1}{2}}|^2 + |H_{\frac{1}{2},+1,0}^{T,-\frac{1}{2}}|^2 + |H_{-\frac{1}{2},+1,-1}^{T,-\frac{1}{2}}|^2 + |H_{\frac{1}{2},+1,-1}^{T,\frac{1}{2}}|^2 \right. \\ &+ \left. |H_{-\frac{1}{2},t,0}^{T,-\frac{1}{2}}|^2 + |H_{\frac{1}{2},t,0}^{T,\frac{1}{2}}|^2 + |H_{-\frac{1}{2},t,-1}^{T,\frac{1}{2}}|^2 + |H_{\frac{1}{2},t,+1}^{T,-\frac{1}{2}}|^2 \right) \Big\} \Big] \quad (8.27) \end{aligned}$$

$$\begin{aligned} \frac{d\Gamma_{\Lambda_c=+1/2}}{dq^2} &= \frac{3N}{2} \left[4|H_{\frac{1}{2},0}^{\text{SP}}|^2 + \frac{8}{3} \left(|H_{\frac{1}{2},0}^{\text{VA}}|^2 + |H_{\frac{1}{2},+1}^{\text{VA}}|^2 \right) + \frac{16}{3} \left(|H_{\frac{1}{2},+1,0}^{T,-\frac{1}{2}}|^2 + |H_{\frac{1}{2},+1,-1}^{T,\frac{1}{2}}|^2 + |H_{\frac{1}{2},t,0}^{T,\frac{1}{2}}|^2 + |H_{\frac{1}{2},t,+1}^{T,-\frac{1}{2}}|^2 \right) \right. \\ &- \frac{32}{3} \text{Re} \left[H_{\frac{1}{2},+1,0}^{T,-\frac{1}{2}*} H_{\frac{1}{2},t,+1}^{T,-\frac{1}{2}} + H_{\frac{1}{2},+1,-1}^{T,\frac{1}{2}*} H_{\frac{1}{2},t,0}^{T,\frac{1}{2}} \right] \\ &+ \frac{m_\ell}{\sqrt{q^2}} \left\{ 8\text{Re} \left[H_{\frac{1}{2},0}^{\text{SP}*} H_{\frac{1}{2},t}^{\text{VA}} \right] + 16\text{Re} \left[H_{\frac{1}{2},0}^{\text{VA}*} H_{\frac{1}{2},t,0}^{T,\frac{1}{2}} + H_{\frac{1}{2},+1}^{\text{VA}*} H_{\frac{1}{2},t,+1}^{T,-\frac{1}{2}} - H_{\frac{1}{2},0}^{\text{VA}*} H_{\frac{1}{2},+1,-1}^{T,\frac{1}{2}} - H_{\frac{1}{2},+1,0}^{T,-\frac{1}{2}} H_{\frac{1}{2},+1}^{\text{VA}*} \right] \right\} \\ &+ \frac{m_\ell^2}{q^2} \left\{ 4|H_{\frac{1}{2},t}^{\text{VA}}|^2 + \frac{4}{3} \left(|H_{\frac{1}{2},0}^{\text{VA}}|^2 + |H_{\frac{1}{2},+1}^{\text{VA}}|^2 \right) \right. \\ &+ \frac{32}{3} \left(|H_{\frac{1}{2},+1,0}^{T,-\frac{1}{2}}|^2 + |H_{\frac{1}{2},+1,-1}^{T,\frac{1}{2}}|^2 + |H_{\frac{1}{2},t,0}^{T,\frac{1}{2}}|^2 + |H_{\frac{1}{2},t,+1}^{T,-\frac{1}{2}}|^2 \right) \\ &- \left. \frac{64}{3} \text{Re} \left[H_{\frac{1}{2},+1,0}^{T,-\frac{1}{2}*} H_{\frac{1}{2},t,+1}^{T,-\frac{1}{2}} - H_{\frac{1}{2},+1,-1}^{T,\frac{1}{2}*} H_{\frac{1}{2},t,0}^{T,\frac{1}{2}} \right] \right\} \Big] \quad (8.28) \end{aligned}$$

$$\begin{aligned}
\frac{d\Gamma_{\Lambda_c=-1/2}}{dq^2} = & \frac{3N}{2} \left[4|H_{-\frac{1}{2},0}^{\text{SP}}|^2 + \frac{8}{3} \left(|H_{-\frac{1}{2},0}^{\text{VA}}|^2 + |H_{-\frac{1}{2},-1}^{\text{VA}}|^2 \right) \right. \\
& + \frac{16}{3} \left(|H_{-\frac{1}{2},-1,0}^{T,\frac{1}{2}}|^2 + |H_{-\frac{1}{2},+1,-1}^{T,-\frac{1}{2}}|^2 + |H_{-\frac{1}{2},t,0}^{T,-\frac{1}{2}}|^2 + |H_{-\frac{1}{2},t,-1}^{T,\frac{1}{2}}|^2 \right) \\
& + \frac{32}{3} \text{Re} \left[\left(H_{-\frac{1}{2},-1,0}^{T,\frac{1}{2}*} H_{-\frac{1}{2},t,-1}^{T,\frac{1}{2}} - H_{-\frac{1}{2},+1,-1}^{T,-\frac{1}{2}*} H_{-\frac{1}{2},t,0}^{T,-\frac{1}{2}} \right) \right] \\
& + \frac{m_\ell}{\sqrt{q^2}} \left\{ 8 \text{Re} \left[H_{-\frac{1}{2},0}^{\text{SP}*} H_{-\frac{1}{2},t}^{\text{VA}} \right] \right. \\
& + 16 \text{Re} \left[H_{-\frac{1}{2},0}^{\text{VA}*} H_{-\frac{1}{2},t,0}^{T,-\frac{1}{2}} - H_{-\frac{1}{2},0}^{\text{VA}*} H_{-\frac{1}{2},+1,-1}^{T,-\frac{1}{2}} + H_{-\frac{1}{2},-1,0}^{T,\frac{1}{2}} H_{-\frac{1}{2},-1}^{\text{VA}*} + H_{-\frac{1}{2},-1}^{\text{VA}*} H_{-\frac{1}{2},t,-1}^{T,\frac{1}{2}} \right] \left. \right\} \\
& + \frac{m_\ell^2}{q^2} \left\{ 4|H_{-\frac{1}{2},t}^{\text{VA}}|^2 + \frac{4}{3} \left(|H_{-\frac{1}{2},0}^{\text{VA}}|^2 + |H_{-\frac{1}{2},-1}^{\text{VA}}|^2 \right) \right. \\
& + \frac{32}{3} \left(|H_{-\frac{1}{2},-1,0}^{T,\frac{1}{2}}|^2 + |H_{-\frac{1}{2},+1,-1}^{T,-\frac{1}{2}}|^2 + |H_{-\frac{1}{2},t,0}^{T,-\frac{1}{2}}|^2 + |H_{-\frac{1}{2},t,-1}^{T,\frac{1}{2}}|^2 \right) \\
& \left. + \frac{64}{3} \text{Re} \left[H_{-\frac{1}{2},-1,0}^{T,\frac{1}{2}*} H_{-\frac{1}{2},t,-1}^{T,\frac{1}{2}} - H_{-\frac{1}{2},+1,-1}^{T,-\frac{1}{2}*} H_{-\frac{1}{2},t,0}^{T,-\frac{1}{2}} \right] \right\} \quad (8.29)
\end{aligned}$$

$$\begin{aligned}
C_F^\ell(q^2) = & \left(\frac{d\Gamma}{dq^2} \right)^{-1} \times \frac{3N}{4} \left(1 - \frac{m_\ell^2}{q^2} \right) \left\{ 4 \left(|H_{-\frac{1}{2},-1}^{\text{VA}}|^2 + |H_{\frac{1}{2},+1}^{\text{VA}}|^2 \right) - 8 \left(|H_{-\frac{1}{2},0}^{\text{VA}}|^2 + |H_{\frac{1}{2},0}^{\text{VA}}|^2 \right) \right. \\
& - 16 \left(|H_{-\frac{1}{2},t,-1}^{T,\frac{1}{2}}|^2 + |H_{\frac{1}{2},t,+1}^{T,-\frac{1}{2}}|^2 + |H_{-\frac{1}{2},-1,0}^{T,\frac{1}{2}}|^2 + |H_{\frac{1}{2},+1,0}^{T,-\frac{1}{2}}|^2 \right) \\
& + 32 \left(|H_{-\frac{1}{2},+1,-1}^{T,-\frac{1}{2}}|^2 + |H_{\frac{1}{2},+1,-1}^{T,\frac{1}{2}}|^2 + |H_{-\frac{1}{2},t,0}^{T,-\frac{1}{2}}|^2 + |H_{\frac{1}{2},t,0}^{T,\frac{1}{2}}|^2 \right) \\
& \left. + 32 \text{Re} \left[H_{\frac{1}{2},+1,0}^{T,-\frac{1}{2}*} H_{\frac{1}{2},t,+1}^{T,-\frac{1}{2}} - H_{-\frac{1}{2},-1,0}^{T,\frac{1}{2}*} H_{-\frac{1}{2},t,-1}^{T,\frac{1}{2}} \right] - 64 \text{Re} \left[H_{-\frac{1}{2},+1,-1}^{T,-\frac{1}{2}*} H_{-\frac{1}{2},t,0}^{T,-\frac{1}{2}} + H_{\frac{1}{2},+1,-1}^{T,\frac{1}{2}*} H_{\frac{1}{2},t,0}^{T,\frac{1}{2}} \right] \right\} \quad (8.30)
\end{aligned}$$

8.4 BGL Parametrization: Outer function in HQET basis

The outer functions $\phi_i(z)$ has the form-

$$\begin{aligned}
\phi_{F_0} = & \frac{8}{M} \sqrt{\frac{n_I}{\pi\chi^L(0)}} \frac{r^{3/2}(1+z)^2(1-z)^2}{\left((1+r)(1-z) + 2\sqrt{r}(1+z) \right)^4} \quad (8.31) \\
\phi_{F_1} = & \frac{16\sqrt{2}}{M} \sqrt{\frac{n_I}{3\pi\chi^T(0)}} \frac{r^{3/2}(1+z)(1-z)^{1/2}}{\left((1+r)(1-z) + 2\sqrt{r}(1+z) \right)^4} \\
\phi_{H_V} = & \frac{16r^{3/2}}{M^2} \sqrt{\frac{n_I}{3\pi\chi^T(0)}} \frac{(1+z)(1-z)^{3/2}}{\left((1+r)(1-z) + 2\sqrt{r}(1+z) \right)^5} \\
\phi_{G_0} = & \frac{16r^{3/2}}{M} \sqrt{\frac{n_I}{\pi\chi^L(0)}} \frac{(1+z)(1-z)^{1/2}}{\left((1+r)(1-z) + 2\sqrt{r}(1+z) \right)^4} \\
\phi_{G_1} = & \frac{8\sqrt{2}r^{3/2}}{M} \sqrt{\frac{n_I}{3\pi\chi^T(0)}} \frac{(1+z)^2(1-z)^{1/2}}{\left((1+r)(1-z) + 2\sqrt{r}(1+z) \right)^4}
\end{aligned}$$

Scenarios	Observables/Predictions					
	$R(D)$	$R(D^*)$	$R(\Lambda_c)$	$F_L^{D^*}$	$P_\tau^{D^*}$	P_τ^D
$\text{Re}[C_{S_1}], \text{Re}[C_{S_2}]$	0.354(29)	0.275(19)	0.354(19)	0.448(30)	-0.463(77)	0.421(47)
$\text{Re}[C_{S_1}], \text{Re}[C_T]$	0.355(29)	0.272(20)	0.361(24)	0.429(11)	-0.496(14)	0.435(43)
$\text{Re}[C_{S_2}], \text{Re}[C_T]$	0.359(28)	0.275(18)	0.318(19)	0.407(44)	-0.076(38)	0.196(81)
$\text{Re}[C_{V_1}], \text{Re}[C_T]$	0.363(29)	0.273(20)	0.345(24)	0.4304(90)	-0.5319(95)	0.306(18)
$\text{Re}[C_{V_2}], \text{Re}[C_T]$	0.339(29)	0.271(20)	0.374(27)	0.402(17)	-0.474(28)	0.354(14)
$\text{Re}[C_{V_1}], \text{Re}[C_{V_2}]$	0.352(29)	0.277(20)	0.360(18)	0.4291(94)	-0.5197(66)	0.3238(27)
$\text{Re}[C_{S_1}], \text{Re}[C_{V_1}]$	0.353(29)	0.277(20)	0.359(19)	0.430(10)	-0.511(13)	0.378(76)
$\text{Re}[C_{S_1}], \text{Re}[C_{V_2}]$	0.353(29)	0.277(20)	0.359(18)	0.4370(100)	-0.499(11)	0.455(47)
$\text{Re}[C_{S_2}], \text{Re}[C_{V_1}]$	0.353(29)	0.277(20)	0.359(19)	0.4244(97)	-0.526(12)	0.373(68)
$\text{Re}[C_{S_2}], \text{Re}[C_{V_2}]$	0.353(29)	0.277(20)	0.358(18)	0.4231(94)	-0.5387(92)	0.472(52)
Measurement	0.357(29)	0.284(13)	0.242(76)	0.430(70)	-0.38(54)	N.A

Table 14: Predictions of $R(D)$, $R(D^*)$, $R(\Lambda_c)$, $F_L^{D^*}$ in the two operator scenarios considering different new physics in τ channel.

$$\phi_{H_A} = \frac{8r^{3/2}}{M^2} \sqrt{\frac{n_I}{3\pi\chi^T(0)}} \frac{(1+z)^2(1-z)^{3/2}}{\left((1+r)(1-z) + 2\sqrt{r}(1+z)\right)^5}$$

where, $r = \frac{m_{\Lambda_c}}{m_{\Lambda_b}}$, n_I , is an isospin Clebsch-Gordan factor, which is 1.0 for $\Lambda_b \rightarrow \Lambda_c$ transition.

$$\begin{aligned}
F_0 &= (M - m)f_0^{lat} \\
H_V &= (M + m)f_+^{lat} \\
F_1 &= f_\perp^{lat} \\
G_0 &= (M + m)g_0^{lat} \\
H_A &= (M - m)g_+^{lat} \\
G_1 &= g_\perp^{lat}
\end{aligned} \tag{8.32}$$

Satisfy the kinematic constrain: $H_A(t_-) = (M - m)G_1(t_-)$, $(M + m)F_0(0) = (M - m)H_V(0)$, $(M - m)G_0(0) = (M + m)H_A(0)$.

8.5 Transformation: Helicity basis to Transversality basis

As in [49] the transformations are not given for how the helicity amplitudes are changed into transversity amplitudes, especially for the tensors which are non-trivial. We assumed the transformation is as the following

$$A_{\perp,0}^T = \frac{1}{\sqrt{2}}(H_{1/2,t,0}^{T,1/2} + H_{1/2,-1,+1}^{T,1/2} + H_{-1/2,-1,1}^{T,-1/2} + H_{-1/2,t,0}^{T,-1/2}) \tag{8.33}$$

$$A_{\parallel,0}^T = \frac{1}{\sqrt{2}}(H_{-1/2,-1,+1}^{T,-1/2} + H_{-1/2,t,0}^{T,-1/2} - (H_{1/2,t,0}^{T,1/2} + H_{1/2,-1,1}^{T,1/2})) \tag{8.34}$$

$$A_{\parallel,1}^T = \frac{1}{\sqrt{2}}(H_{-1/2,-1,0}^{T,1/2} + H_{-1/2,t,-1}^{T,1/2} - (H_{1/2,0,1}^{T,-1/2} + H_{1/2,t,1}^{T,-1/2})) \tag{8.35}$$

Obs.	[C_{S_1}, C_{S_2}]	[C_{S_1}, C_T]	[C_{S_2}, C_T]	[C_{V_1}, C_{V_2}]	[C_{V_1}, C_T]	[C_{V_2}, C_T]	[C_{S_1}, C_{V_1}]	[C_{S_1}, C_{V_2}]	[C_{S_2}, C_{V_1}]	[C_{S_2}, C_{V_2}]	SM
\hat{K}_{1cc}	0.311(2)	0.3137(15)	0.2999(25)	0.3116(14)	0.3099(26)	0.3132(13)	0.3125(15)	0.3137(15)	0.3123(14)	0.3136(15)	0.3120(25)
\hat{K}_{1ss}	0.3447(8)	0.34315(74)	0.3501(13)	0.34418(69)	0.3451(13)	0.34342(63)	0.34375(75)	0.34313(73)	0.34386(69)	0.34319(73)	0.34399(65)
\hat{K}_{2cc}	0.202(22)	0.200(25)	-0.018(29)	-0.210(23)	0.223(26)	0.178(25)	0.208(22)	0.205(22)	0.206(22)	0.197(22)	0.208(22)
\hat{K}_{2ss}	0.237(26)	0.229(28)	-0.0082(345)	-0.243(26)	0.258(30)	0.205(29)	0.240(26)	0.235(26)	0.238(26)	0.227(25)	0.240(26)
\hat{K}_{3sc}	0.0182(25)	0.0157(23)	0.0054(39)	-0.0173(23)	0.0183(26)	0.0143(26)	0.0167(23)	0.0158(22)	0.0169(23)	0.0159(22)	0.0172(23)
\hat{K}_{3s}	0.131(19)	0.0359(92)	-0.010(20)	0.132(18)	0.037(10)	0.030(14)	0.039(10)	0.041(12)	0.038(10)	0.042(12)	0.0436(81)
A_{FB}^f	-0.303(17)	0.119(12)	-0.081(28)	0.3770(90)	0.101(12)	0.121(13)	0.111(15)	0.118(12)	0.106(11)	0.104(11)	0.103(11)
A_{FB}^{Acf}	-0.169(18)	0.0248(88)	0.0201(75)	-0.195(21)	0.0240(71)	0.0169(75)	0.0234(89)	0.0253(80)	0.0213(71)	0.0201(74)	0.0184(62)
A_{FB}^{Ae}	0.338(37)	0.329(41)	-0.017(49)	-0.348(38)	0.370(43)	0.294(42)	0.344(37)	0.337(37)	0.341(37)	0.326(36)	0.344(37)
P_{Ae}	-0.757(22)	-0.725(49)	0.065(109)	0.772(18)	-0.830(51)	-0.647(62)	-0.761(12)	-0.742(21)	-0.754(18)	-0.712(27)	-0.761(12)
$P^{(Ae)}$	-0.218(47)	-0.196(36)	0.098(37)	-0.244(25)	-0.245(24)	-0.214(35)	-0.224(51)	-0.196(35)	-0.236(35)	-0.220(31)	-0.258(16)
C_F^f	-0.102(8)	-0.088(7)	-0.151(11)	-0.098(6)	-0.106(12)	-0.091(6)	-0.094(7)	-0.088(7)	-0.095(6)	-0.089(7)	-0.096(6)

Table 15: Predictions of angular observables with the two operator scenarios fit results.

$$A_{\perp,1}^T = \frac{1}{\sqrt{2}}(H_{-1/2,-1,0}^{T,1/2} + H_{-1/2,t,-1}^{T,1/2} + (H_{1/2,0,1}^{T,-1/2} + H_{1/2,t,1}^{T,-1/2})) \quad (8.36)$$

and for the vector amplitudes the transformation looks like

$$A_{\perp,1} = \frac{1}{\sqrt{2}}(H_{1/2,1}^{VA} - H_{-1/2,-1}^{VA}) \quad (8.37)$$

$$A_{\parallel,1} = \frac{1}{\sqrt{2}}(H_{1/2,1}^{VA} + H_{-1/2,-1}^{VA}) \quad (8.38)$$

$$A_{\perp,0} = \frac{1}{\sqrt{2}}(H_{1/2,0}^{VA} - H_{-1/2,0}^{VA}) \quad (8.39)$$

$$A_{\parallel,0} = \frac{1}{\sqrt{2}}(H_{1/2,0}^{VA} + H_{-1/2,0}^{VA}) \quad (8.40)$$

$$A_{\perp,t} = \frac{1}{\sqrt{2}}\{(H_{1/2,t}^{VA} - H_{-1/2,t}^{VA}) + \frac{\sqrt{q^2}}{m_l}(H_{1/2,0}^{SP} - H_{-1/2,0}^{SP})\} \quad (8.41)$$

$$A_{\parallel,t} = \frac{1}{\sqrt{2}}\{(H_{1/2,t}^{VA} + H_{-1/2,t}^{VA}) + \frac{\sqrt{q^2}}{m_l}(H_{1/2,0}^{SP} + H_{-1/2,0}^{SP})\}. \quad (8.42)$$

8.6 Theory Inputs

These Analytic expressions have been taken from [10] for our NP analysis.

$$R(D) = (0.304 \pm 0.003) \times (1 + 1.35C_{S_1}^2 + C_{S_1}(2.70C_{S_2} + 1.72C_{V_1} + 1.72C_{V_2} + 1.72) + 1.35C_{S_2}^2 + 0.83C_T C_{V_1} + C_{S_2}(1.72C_{V_1} + 1.72C_{V_2} + 1.72) + 0.83C_T C_{V_2} + (0.49C_T + 0.83)C_T + C_{V_1}^2 + 2.00C_{V_1} C_{V_2} + 2.00C_{V_1} + C_{V_2}^2 + 2.00C_{V_2}) \quad (8.43)$$

$$R(D^*) = (0.258 \pm 0.012) \times (1 + 0.04C_{S_1}^2 + C_{S_1}(-0.07C_{S_2} + 0.10C_{V_1} - 0.10C_{V_2} + 0.10) + 0.04C_{S_2}^2 + C_{S_2}(-0.10C_{V_1} + 0.10C_{V_2} - 0.10) - 2.94C_T C_{V_1} + 4.79C_T C_{V_2} + (10.65C_T - 2.94)C_T + C_{V_1}^2 - 1.79C_{V_1} C_{V_2} + 2.00C_{V_1} + C_{V_2}^2 - 1.79C_{V_2}) \quad (8.44)$$

$$F_L^{D^*} = (0.427 \pm 0.009) \times (27.26 + 2.34C_{S_1}^2 + C_{S_1}(-4.68C_{S_2} + 6.65C_{V_1} - 6.65C_{V_2} + 6.65) + 2.34C_{S_2}^2 - 66.82C_T C_{V_1} + C_{S_2}(-6.65C_{V_1} + 6.65C_{V_2} - 6.65) + 66.82C_T C_{V_2} + C_T(69.62C_T - 66.82) + 27.26C_{V_1}^2 - 54.52C_{V_1} C_{V_2} + 54.52C_{V_1} + 27.26C_{V_2}^2 - 54.26C_{V_2}) / (27.26 + C_{S_1}^2 + C_{S_1}(-2.00C_{S_2} + 2.84C_{V_1} - 2.84C_{V_2} + 2.84) + C_{S_2}^2 + C_{S_2}(-2.84C_{V_1} + 2.84C_{V_2} - 2.84) - 80.15C_T C_{V_1} + 130.72C_T C_{V_2})$$

$$+ C_T(290.34C_T - 80.15) + 27.26C_{V_1}^2 - 48.81C_{V_1}C_{V_2} + 54.52C_{V_1} + 27.26C_{V_2}^2 - 48.81C_{V_2})$$

(8.45)

References

- [1] HEAVY FLAVOR AVERAGING GROUP, HFLAV collaboration, *Averages of b -hadron, c -hadron, and τ -lepton properties as of 2021*, *Phys. Rev. D* **107** (2023) 052008 [2206.07501].
- [2] D. Bigi, P. Gambino and S. Schacht, *A fresh look at the determination of $|V_{cb}|$ from $B \rightarrow D^* \ell \nu$* , *Phys. Lett. B* **769** (2017) 441 [1703.06124].
- [3] S. Jaiswal, S. Nandi and S. K. Patra, *Extraction of $|V_{cb}|$ from $B \rightarrow D^{(*)} \ell \nu_\ell$ and the Standard Model predictions of $R(D^{(*)})$* , *JHEP* **12** (2017) 060 [1707.09977].
- [4] P. Gambino, M. Jung and S. Schacht, *The V_{cb} puzzle: An update*, *Phys. Lett. B* **795** (2019) 386 [1905.08209].
- [5] S. Jaiswal, S. Nandi and S. K. Patra, *Updates on extraction of $|V_{cb}|$ and SM prediction of $R(D^*)$ in $B \rightarrow D^* \ell \nu_\ell$ decays*, *JHEP* **06** (2020) 165 [2002.05726].
- [6] S. Iguro and R. Watanabe, *Bayesian fit analysis to full distribution data of $\bar{B} \rightarrow D^{(*)} \ell \bar{\nu} : |V_{cb}|$ determination and new physics constraints*, *JHEP* **08** (2020) 006 [2004.10208].
- [7] A. Biswas, S. Nandi and I. Ray, *Extractions of $|V_{ub}|/|V_{cb}|$ from a combined study of the exclusive $b \rightarrow u(c) \ell^- \bar{\nu}_\ell$ decays*, *JHEP* **07** (2023) 024 [2212.02528].
- [8] G. Martinelli, S. Simula and L. Vittorio, *$|V_{cb}|$ and $R(D^{(*)})$ using lattice QCD and unitarity*, *Phys. Rev. D* **105** (2022) 034503 [2105.08674].
- [9] G. Martinelli, S. Simula and L. Vittorio, *Exclusive determinations of $|V_{cb}|$ and $R(D^*)$ through unitarity*, *Eur. Phys. J. C* **82** (2022) 1083 [2109.15248].
- [10] I. Ray and S. Nandi, *Test of new physics effects in $\bar{B} \rightarrow (D^{(*)}, \pi) \ell^- \bar{\nu}_\ell$ decays with heavy and light leptons*, *2305.11855*.
- [11] S. Fajfer, J. F. Kamenik, I. Nisandzic and J. Zupan, *Implications of Lepton Flavor Universality Violations in B Decays*, *Phys. Rev. Lett.* **109** (2012) 161801 [1206.1872].
- [12] A. Datta, M. Duraisamy and D. Ghosh, *Diagnosing New Physics in $b \rightarrow c \tau \nu_\tau$ decays in the light of the recent BaBar result*, *Phys. Rev. D* **86** (2012) 034027 [1206.3760].
- [13] S. Bhattacharya, S. Nandi and S. K. Patra, *Looking for possible new physics in $B \rightarrow D^{(*)} \tau \nu_\tau$ in light of recent data*, *Phys. Rev. D* **95** (2017) 075012 [1611.04605].
- [14] D. Bardhan, P. Byakti and D. Ghosh, *A closer look at the R_D and R_{D^*} anomalies*, *JHEP* **01** (2017) 125 [1610.03038].
- [15] A. Celis, M. Jung, X.-Q. Li and A. Pich, *Scalar contributions to $b \rightarrow c(u) \tau \nu$ transitions*, *Phys. Lett. B* **771** (2017) 168 [1612.07757].
- [16] Z.-R. Huang, Y. Li, C.-D. Lu, M. A. Paracha and C. Wang, *Footprints of New Physics in $b \rightarrow c \tau \nu$ Transitions*, *Phys. Rev. D* **98** (2018) 095018 [1808.03565].
- [17] A. Azatov, D. Bardhan, D. Ghosh, F. Sgarlata and E. Venturini, *Anatomy of $b \rightarrow c \tau \nu$ anomalies*, *JHEP* **11** (2018) 187 [1805.03209].
- [18] S. Bhattacharya, S. Nandi and S. Kumar Patra, *$b \rightarrow c \tau \nu_\tau$ Decays: a catalogue to compare, constrain, and correlate new physics effects*, *Eur. Phys. J. C* **79** (2019) 268 [1805.08222].
- [19] Z.-R. Huang, Y. Li, C.-D. Lu, M. A. Paracha and C. Wang, *Footprints of new physics in $b \rightarrow c \tau \nu$ transitions*, *Phys. Rev. D* **98** (2018) 095018.
- [20] A. Angelescu, D. Bećirević, D. A. Faroughy and O. Sumensari, *Closing the window on single leptoquark solutions to the B -physics anomalies*, *JHEP* **10** (2018) 183 [1808.08179].
- [21] S. Iguro, Y. Omura and M. Takeuchi, *Test of the $R(D^{(*)})$ anomaly at the LHC*, *Phys. Rev. D* **99** (2019) 075013 [1810.05843].

- [22] C. Murgui, A. Peñuelas, M. Jung and A. Pich, *Global fit to $b \rightarrow c\tau\nu$ transitions*, *JHEP* **09** (2019) 103 [[1904.09311](#)].
- [23] R.-X. Shi, L.-S. Geng, B. Grinstein, S. Jäger and J. Martin Camalich, *Revisiting the new-physics interpretation of the $b \rightarrow c\tau\nu$ data*, *JHEP* **12** (2019) 065 [[1905.08498](#)].
- [24] D. Bečirević, M. Fedele, I. Nišandžić and A. Tayduganov, *Lepton Flavor Universality tests through angular observables of $\bar{B} \rightarrow D^{(*)}\ell\bar{\nu}$ decay modes*, [1907.02257](#).
- [25] A. Biswas, L. Mukherjee, S. Nandi and S. K. Patra, *Constraining New Physics with Possible Dark Matter Signatures from a Global CKM Fit*, [2111.01176](#).
- [26] S. Iguro, T. Kitahara and R. Watanabe, *Global fit to $b \rightarrow c\tau\nu$ anomalies 2022 mid-autumn*, [2210.10751](#).
- [27] A. Bhatta and R. Mohanta, *Delving into new physics in semileptonic $b \rightarrow c\tau\nu$ transitions*, *Int. J. Mod. Phys. A* **38** (2023) 2350148.
- [28] BABAR collaboration, *Evidence for an excess of $\bar{B} \rightarrow D^{(*)}\tau^-\bar{\nu}_\tau$ decays*, *Phys. Rev. Lett.* **109** (2012) 101802 [[1205.5442](#)].
- [29] BABAR collaboration, *Measurement of an Excess of $\bar{B} \rightarrow D^{(*)}\tau^-\bar{\nu}_\tau$ Decays and Implications for Charged Higgs Bosons*, *Phys. Rev. D* **88** (2013) 072012 [[1303.0571](#)].
- [30] BELLE collaboration, *Measurement of the branching ratio of $\bar{B} \rightarrow D^{(*)}\tau^-\bar{\nu}_\tau$ relative to $\bar{B} \rightarrow D^{(*)}\ell^-\bar{\nu}_\ell$ decays with hadronic tagging at Belle*, *Phys. Rev. D* **92** (2015) 072014 [[1507.03233](#)].
- [31] LHCb collaboration, *Measurement of the ratio of branching fractions $\mathcal{B}(\bar{B}^0 \rightarrow D^{*+}\tau^-\bar{\nu}_\tau)/\mathcal{B}(\bar{B}^0 \rightarrow D^{*+}\mu^-\bar{\nu}_\mu)$* , *Phys. Rev. Lett.* **115** (2015) 111803 [[1506.08614](#)].
- [32] BELLE collaboration, *Measurement of the branching ratio of $\bar{B}^0 \rightarrow D^{*+}\tau^-\bar{\nu}_\tau$ relative to $\bar{B}^0 \rightarrow D^{*+}\ell^-\bar{\nu}_\ell$ decays with a semileptonic tagging method*, *Phys. Rev. D* **94** (2016) 072007 [[1607.07923](#)].
- [33] BELLE collaboration, *Measurement of the τ lepton polarization and $R(D^*)$ in the decay $\bar{B} \rightarrow D^*\tau^-\bar{\nu}_\tau$* , *Phys. Rev. Lett.* **118** (2017) 211801 [[1612.00529](#)].
- [34] BELLE collaboration, *Measurement of the τ lepton polarization and $R(D^*)$ in the decay $\bar{B} \rightarrow D^*\tau^-\bar{\nu}_\tau$ with one-prong hadronic τ decays at Belle*, *Phys. Rev. D* **97** (2018) 012004 [[1709.00129](#)].
- [35] LHCb collaboration, *Test of Lepton Flavor Universality by the measurement of the $B^0 \rightarrow D^{*-}\tau^+\nu_\tau$ branching fraction using three-prong τ decays*, *Phys. Rev. D* **97** (2018) 072013 [[1711.02505](#)].
- [36] LHCb collaboration, *Measurement of the ratio of the $B^0 \rightarrow D^{*-}\tau^+\nu_\tau$ and $B^0 \rightarrow D^{*-}\mu^+\nu_\mu$ branching fractions using three-prong τ -lepton decays*, *Phys. Rev. Lett.* **120** (2018) 171802 [[1708.08856](#)].
- [37] BELLE collaboration, *Measurement of $\mathcal{R}(D)$ and $\mathcal{R}(D^*)$ with a semileptonic tagging method*, *Phys. Rev. Lett.* **124** (2020) 161803 [[1910.05864](#)].
- [38] LHCb collaboration, *Measurement of the ratios of branching fractions $\mathcal{R}(D^*)$ and $\mathcal{R}(D^0)$* , [2302.02886](#).
- [39] M. Fedele, M. Blanke, A. Crivellin, S. Iguro, T. Kitahara, U. Nierste et al., *Impact of $\Lambda_b \rightarrow \Lambda c\tau\nu$ measurement on new physics in $b \rightarrow cl\nu$ transitions*, *Phys. Rev. D* **107** (2023) 055005 [[2211.14172](#)].
- [40] W. Detmold, C. Lehner and S. Meinel, *$\Lambda_b \rightarrow p\ell^-\bar{\nu}_\ell$ and $\Lambda_b \rightarrow \Lambda_c\ell^-\bar{\nu}_\ell$ form factors from lattice QCD with relativistic heavy quarks*, *Phys. Rev. D* **92** (2015) 034503 [[1503.01421](#)].
- [41] S. Shivashankara, W. Wu and A. Datta, *$\Lambda_b \rightarrow \Lambda_c\tau\bar{\nu}_\tau$ Decay in the Standard Model and with New Physics*, *Phys. Rev. D* **91** (2015) 115003 [[1502.07230](#)].
- [42] X.-Q. Li, Y.-D. Yang and X. Zhang, *$\Lambda_b \rightarrow \Lambda_c\tau\bar{\nu}_\tau$ decay in scalar and vector leptoquark scenarios*, *JHEP* **02** (2017) 068 [[1611.01635](#)].
- [43] A. Datta, S. Kamali, S. Meinel and A. Rashed, *Phenomenology of $\Lambda_b \rightarrow \Lambda_c\tau\bar{\nu}_\tau$ using lattice QCD calculations*, *JHEP* **08** (2017) 131 [[1702.02243](#)].

- [44] E. Di Salvo, F. Fontanelli and Z. J. Ajaltouni, *Detailed Study of the Decay $\Lambda_b \rightarrow \Lambda_c \tau \bar{\nu}_\tau$* , *Int. J. Mod. Phys. A* **33** (2018) 1850169 [[1804.05592](#)].
- [45] A. Ray, S. Sahoo and R. Mohanta, *Probing new physics in semileptonic Λ_b decays*, *Phys. Rev. D* **99** (2019) 015015 [[1812.08314](#)].
- [46] N. Penalva, E. Hernández and J. Nieves, *Further tests of lepton flavour universality from the charged lepton energy distribution in $b \rightarrow c$ semileptonic decays: The case of $\Lambda_b \rightarrow \Lambda_c \ell \bar{\nu}_\ell$* , *Phys. Rev. D* **100** (2019) 113007 [[1908.02328](#)].
- [47] M. Ferrillo, A. Mathad, P. Owen and N. Serra, *Probing effects of new physics in $\Lambda_b^0 \rightarrow \Lambda_c^+ \mu^- \bar{\nu}_\mu$ decays*, *JHEP* **12** (2019) 148 [[1909.04608](#)].
- [48] X.-L. Mu, Y. Li, Z.-T. Zou and B. Zhu, *Investigation of effects of new physics in $\Lambda_b \rightarrow \Lambda_c \tau \bar{\nu}_\tau$ decay*, *Phys. Rev. D* **100** (2019) 113004 [[1909.10769](#)].
- [49] P. Böer, A. Kokulu, J.-N. Toelstede and D. van Dyk, *Angular Analysis of $\Lambda_b \rightarrow \Lambda_c(\rightarrow \Lambda \pi) \ell \bar{\nu}$* , *JHEP* **12** (2019) 082 [[1907.12554](#)].
- [50] D. Bečirević and F. Jaffredo, *Looking for the effects of New Physics in the $\Lambda_b \rightarrow \Lambda_c(\rightarrow \Lambda \pi) \ell \nu$ decay mode*, [2209.13409](#).
- [51] S. Karmakar, S. Chattopadhyay and A. Dighe, *Identifying physics beyond SMEFT in the angular distribution of $\Lambda_b \rightarrow \Lambda_c(\rightarrow \Lambda \pi) \tau \bar{\nu}_\tau$ decay*, [2305.16007](#).
- [52] LHCb collaboration, *Observation of the decay $\Lambda_b^0 \rightarrow \Lambda_c^+ \tau^- \bar{\nu}_\tau$* , *Phys. Rev. Lett.* **128** (2022) 191803 [[2201.03497](#)].
- [53] LHCb collaboration, *Measurement of the D^* longitudinal polarization in $B^0 \rightarrow D^{*-} \tau^+ \nu_\tau$ decays*, [2311.05224](#).
- [54] C. G. Boyd, B. Grinstein and R. F. Lebed, *Precision corrections to dispersive bounds on form-factors*, *Phys. Rev.* **D56** (1997) 6895 [[hep-ph/9705252](#)].
- [55] C. Bourrely, I. Caprini and L. Lellouch, *Model-independent description of $B \rightarrow \pi l \nu$ decays and a determination of $-V_{ub}$* , *Phys. Rev. D* **79** (2009) 013008 [[0807.2722](#)].
- [56] PARTICLE DATA GROUP collaboration, *Review of Particle Physics*, *PTEP* **2022** (2022) 083C01.
- [57] S. K. Patra, *OptEx*, 2019.
- [58] HFLAV collaboration, *Averages of b -hadron, c -hadron, and τ -lepton properties as of 2021*, *Phys. Rev. D* **107** (2023) 052008 [[2206.07501](#)].
- [59] DELPHI collaboration, *Measurement of the Λ_b^0 decay form-factor*, *Phys. Lett. B* **585** (2004) 63 [[hep-ex/0403040](#)].
- [60] LHCb collaboration, *Measurement of the ratio of branching fractions $\mathcal{B}(B_c^+ \rightarrow J/\psi \tau^+ \nu_\tau) / \mathcal{B}(B_c^+ \rightarrow J/\psi \mu^+ \nu_\mu)$* , *Phys. Rev. Lett.* **120** (2018) 121801 [[1711.05623](#)].
- [61] CMS collaboration, *Test of lepton flavor universality violation in semileptonic B_c^+ meson decays at CMS*, .
- [62] LATTICE-HPQCD collaboration, *$R(J/\psi)$ and $B_c^- \rightarrow J/\psi \ell^- \bar{\nu}_\ell$ Lepton Flavor Universality Violating Observables from Lattice QCD*, *Phys. Rev. Lett.* **125** (2020) 222003 [[2007.06956](#)].
- [63] MILC collaboration, *$B \rightarrow D \ell \nu$ form factors at nonzero recoil and $-V_{cb}$ from 2+1-flavor lattice QCD*, *Phys. Rev. D* **92** (2015) 034506 [[1503.07237](#)].
- [64] HPQCD collaboration, *$B \rightarrow D \ell \nu$ form factors at nonzero recoil and extraction of $|V_{cb}|$* , *Phys. Rev. D* **92** (2015) 054510 [[1505.03925](#)].
- [65] FERMILAB LATTICE, MILC, FERMILAB LATTICE, MILC collaboration, *Semileptonic form factors for $B \rightarrow D^* \ell \nu$ at nonzero recoil from 2+1-flavor lattice QCD: Fermilab Lattice and MILC Collaborations*, *Eur. Phys. J. C* **82** (2022) 1141 [[2105.14019](#)].

[66] JLQCD collaboration, $B \rightarrow D^* \ell \nu_\ell$ semileptonic form factors from lattice QCD with Möbius domain-wall quarks, [2306.05657](#).